Analysis of Rod/Cone Gap Junctions from the Reconstruction of Mouse Photoreceptor Terminals

Munenori Ishibashi[1], Joyce Keung[1], Catherine W. Morgans[2], Sue A. Aicher[2], James R. Carroll[2], Joshua H. Singer[3], Li Jia[4], Wei Li[4], Iris Fahrenfort[1], Christophe P. Ribelayga[1,5], Stephen C. Massey[1,5]

[1] Richard Ruiz Department of Ophthalmology and Visual Science, McGovern Medical School, University of Texas at Houston, Houston TX 77030

[2] Department of Chemical Physiology & Biochemistry, Oregon Health & Science University, Portland, OR 97239

[3] Department of Biology, University of Maryland, College Park, United States.

[4] Retinal Neurophysiology Section, National Eye Institute, National Institutes of Health, USA.

[5] To whom correspondence should be addressed

Contributions

The project was designed by SCM, MI, IF and CPR; JS contributed an SBF-SEM dataset; CWM, SAA and JRC prepared two FIB-SEM datasets; LJ and WL contributed the blue cone mouse line; MI and SCM performed confocal microscopy and data analysis; JK performed immunocytochemistry; SCM, MI, IF and CPR, first draft and editing; all authors edited and approved final draft.

Acknowledgement

This project was inspired by the paper from Behrens et al (2016) who used e2006 to reconstruct bipolar cells. We thank Christian Behrens, Timm Schubert, Philipp Berens and Thomas Euler (University of Tübingen) for generously sharing data on blue cone bipolar cells. We thank Moritz Helmstaedter (MPI, Frankfurt) for hosting the e2006 dataset. We thank David Berson, Brown University, for advice, encouragement and an introduction to connectomics. We thank Jessica Riesterer at the Multiscale Microscopy Core, an OHSU University Shared Resource core facility, for acquiring the FIB-SEM datasets.

Supported by NIH grants: EY017836 (JHS); EY02948 (SCM & CPR); P30EY028102 (SCM); P30NS061800 (SAA); R01MH127343 (SAA, SCM, CWM, & CPR)

Abstract

Using serial blockface-scanning electron microscopy (SBF-SEM) and focused ion beam-scanning electron microscopy (FIB-SEM), combined with confocal microscopy for the gap junction protein Cx36, we reconstructed mouse photoreceptor terminals and located the gap junctions between them. An exuberant spray of fine telodendria extends from each cone pedicle (including blue cones) to contact 40-50 nearby rod spherules where Cx36 clusters were located, close to the mouth of the synaptic opening. There were approximately 50 Cx36 clusters per cone pedicle and 2-3 per rod spherule. We were unable to detect rod/rod or cone/cone coupling. Thus, rod/cone coupling accounts for nearly all gap junctions between photoreceptors. Our calculations suggest a mean of 82 Cx36 channels between a rod/cone pair of which 25% are open at rest. Rod/cone gap junctions are modulated by dopamine. Comparing our morphological calculations of maximum coupling to previous physiological results suggests that dopamine antagonists can drive rod/cone gap junctions to a surprisingly high open probability, approaching 100%.

53 **Introduction**

54

55 In the mammalian retina, with few exceptions, rods far outnumber cones. Specifically, for the
56 mouse retina, only 3% of the photoreceptors are cones (Carter-Dawson and Lavail, 1979). The
57 synaptic endings of photoreceptors, known as cone pedicles and rod spherules, terminate in the
58 outer plexiform layer (OPL) where they make synaptic connections with second-order neurons,
59 horizontal cells and bipolar cells. In general, the retina is a layered structure and the OPL is no
60 exception. Cone pedicles are found in a single layer in the mid-OPL whereas the smaller rod
61 spherules accumulate in several layers between the cone pedicles and the photoreceptor cell
62 bodies in the top (distal) half of the OPL. Numerically, the OPL is dominated by rod spherules.

63

64 Cone pedicles are the largest structures in the OPL. They contain numerous synaptic ribbons and
65 make contacts with horizontal cells and 13 types of cone bipolar cell. One of these bipolar cell
66 types, cb9, contacts short wavelength-sensitive (i.e. "blue") cones selectively, which can be
67 identified on this basis (Behrens et al., 2016; Nadal-Nicolás et al., 2020). Rod spherules contain
68 a single large ribbon and make synapses with the axon terminals of horizontal cells and with the
69 dendrites of a single type of rod bipolar cell. Each rod bipolar cell contacts ~35 rods (Behrens et
70 al., 2016), forming the most sensitive or primary rod pathway.

71

72 In addition to chemical synapses, there are a large number of small gap junctions in the OPL,
73 which were first described in early ultrastructural studies (Kolb, 1977; Raviola and Gilula, 1973;
74 Smith et al., 1986). Gap junctions mediate electrical coupling between neurons and contain
75 clusters of intercellular channels that allow the passage of ions and other small molecules. At a

76 gap junction, the membranes of two neighboring cells are apposed or "zippered", leaving only a
77 2-4 nm "gap" (Bloomfield and Völgyi, 2009; Miller and Pereda, 2017). Each gap junction
78 channel is formed of two docked hemichannels, or connexons and each connexon is assembled
79 from six connexin subunits. Connexin expression is required on both sides to form a gap junction
80 (Miller et al.,2017; Jin et al., 2020). The vertebrate connexin family in mouse includes 20
81 members, including Cx36, the most common neuronal connexin (Beyer and Berthoud, 2009;
82 Söhl et al., 2004). Gap junctions are widespread in neural tissue and support functions such as
83 signal averaging, noise reduction and synchronization (Connors, 2017; Nagy et al., 2018).
84
85 In lower vertebrates, rods are extensively electrically coupled (Zhang and Wu, 2004) but, in
86 general, this is not the case for mammals. Cone/cone and rod/cone gap junctions have been
87 reported in cat and primate retinae (Kolb, 1977; Smith et al., 1986). Specifically, basal
88 processes, called telodendria, spread laterally from cone pedicles to make small gap junctions
89 with rod spherules. In freeze-fracture electron microscopy (EM), they appear as strings of single
90 particles curved around the synaptic invagination of rod spherules (Raviola and Gilula, 1973).
91 The presence of rod/cone gap junctions at rod/cone contacts is consistent with the transmission
92 of rod signals to cones and cone-driven second order neurons such as horizontal cells and cone
93 bipolar cells (Asteriti et al., 2014; Ingram et al., 2019; Li et al., 2010; Nelson, 1977; Ribelayga et
94 al., 2008; Ribelayga and Mangel, 2010; Schneeweis and Schnapf, 1995). More rarely, rod/rod
95 gap junctions have been suggested from tracer coupling studies and from EM studies of the
96 mouse retina (Jin et al., 2015; Li et al., 2012; Tsukamoto et al., 2001).
97

98 Rods and cones both express Cx36, but no other connexins (Bloomfield and Völgyi, 2009; Jin et
99 al., 2020; O'Brien et al., 2012). Connexin expression is required on both sides of a gap junction
100 and, in fact, Cx36 mediated rod/cone coupling accounts for most of the gap junctions in the OPL
101 (Asteriti et al., 2017; Ingram et al., 2019; Jin et al., 2020; Miller et al., 2017). If indeed rods
102 express Cx36, then it raises the possibility that they could also be coupled via Cx36 gap
103 junctions. However, the evidence for rod/rod gap junctions in the mammalian retina is mixed
104 (Bloomfield and Völgyi, 2009; Jin et al., 2020; Tsukamoto et al., 2001) and will be addressed
105 here. We used a combination of confocal microscopy, serial blockface scanning electron
106 microscopy (SBF-SEM), and focused-ion beam SEM (FIB-SEM) to address four major goals: i)
107 to reconstruct the cone telodendrial network; ii) to identify all gap junction types in the OPL; iii)
108 to resolve the question of rod/rod coupling, and iv) to make a quantitative estimate of rod/cone
109 coupling.
110
111 Gap junctions can be difficult to identify reliably in EM material (Pallotto et al., 2015). For this
112 project, we chose to use a publicly available dataset, e2006 (Helmstaedter et al., 2013), which
113 contains photoreceptor terminals and the OPL, to map membrane contacts between
114 photoreceptors. Unfortunately, because this dataset was prepared to enhance membrane contrast
115 and facilitate tracing neuronal processes, gap junctions are not visible. To work around this
116 problem, we used confocal microscopy to identify the location of Cx36 gap junctions around the
117 synaptic opening of each rod spherule (Jin et al, 2020). Tracing the contacts between cone
118 telodendria and rod spherules revealed numerous potential gap junctions coincident with the
119 location of Cx36. Thus, the combination of confocal microscopy and SBF-SEM is
120 complementary. To confirm the location of rod/cone gap junctions, we used FIB-SEM on new

samples processed to preserve the ultrastructure, which allowed high-resolution imaging of contacts between cone pedicles and rod spherules. In addition, FIB-SEM provides isotropic data (same resolution in each dimension), facilitating 3D reconstruction (Xu et al., 2017) and the measurement of gap junction dimensions.

126 # Results

127

128 **Confocal microscopy: Localization of Cx36 in the OPL**

129

130 Immunofluorescent labeling for Cx36 revealed small clusters of labeling in the OPL (Fig. 1A,
131 red). To locate these potential gap junctions, we used an antibody to the vesicular glutamate
132 transporter (vGlut1) (Fig. 1A, blue) to identify rod spherules and an antibody to cone arrestin to
133 label cone pedicles (Fig. 1A, green). Labeling with the cone arrestin (CAR) antibody stains
134 cones in their entirety from the outer segment to the pedicle (Fig. 1A). Fine processes, called
135 telodendria, extend laterally from each cone pedicle to form an overlapping matrix in the outer
136 plexiform layer (OPL). The area between and above the cone pedicles is filled with numerous
137 vGlut1-labeled rod spherules while the space underneath is occupied by the dendrites of
138 horizontal cells and bipolar cells.

139

140 The cone telodendria rose above the level of the cone pedicles to contact the overlying rod
141 spherules (Fig. 1A). In the OPL, there are many small Cx36 clusters associated with cone
142 telodendria, often at their tips, relatively high (distal) in the OPL. Staining the rod spherules for
143 a synaptic vesicle marker, such as the vesicular glutamate transporter, shows that Cx36 clusters
144 are contained within the band of vGlut1 labeled rod spherules (Fig. 1A, Video 1). There was no
145 Cx36 labeling in the outer nuclear layer (ONL). Cx36 clusters are also apparent underneath each
146 cone pedicle (arrowheads, Fig. 1A), on processes previously identified as bipolar cell dendrites
147 (Feigenspan et al., 2004; O'Brien et al., 2012; Raviola and Gilula, 1973).

148

149 We analyzed these data by plotting the intensity of Cx36 signal against depth in the retina (Fig.
150 1B). The vast majority of Cx36 clusters are contained within the OPL, within the bands of cone
151 arrestin and vGlut1 labeling, which show the position of cone pedicles and rod spherules,
152 respectively. On the left of the curve, there is a minor peak in the Cx36 channel (red line, black
153 arrowhead), which falls outside the cone arrestin curve, corresponding to the Cx36 labeling of
154 bipolar cell dendrites underneath each cone pedicle (Raviola and Gilula, 1973; O'Brien et al.,
155 2012). Because this peak does not colocalize with cones, it was excluded from analysis and is not
156 further considered in this paper. The area under the Cx36 curve indicates that an insignificant
157 fraction (less than 0.2%) of Cx36 clusters are in the ONL. This is important because it rules out
158 the presence of Cx36 gap junctions between rod somas and/or passing axons in the ONL, where
159 they are packed together at high density.
160
161 **EGFP-labeled cones**
162
163 When all the cones are labeled for cone arrestin, the complexity of the overlapping matrix makes
164 it difficult to analyze individual cone pedicles with confidence. Therefore, we turned to a
165 transgenic mouse line, *Opn4*^{cre}*;Z/EG* (Ecker et al., 2010), where there is sparse labeling of a few
166 individual cones (Fig. 1C). This made it possible to view individual EGFP-labeled cones
167 against a background of all cones stained for cone arrestin. The immunofluorescence data were
168 analyzed by extracting only the Cx36 clusters that colocalized with EGFP-labeled pedicles and
169 reconstructing in 3D to find the number and location of Cx36 clusters on a single cone pedicle
170 (Fig. 1D, Video 2). At each Cx36 cluster, there is an adjacent rod spherule (Fig. 1E), suggesting
171 these structures are rod/cone gap junctions. There are approximately 51 $\pm$ 8.9 (mean, $\pm$ SD, n =

172 18) Cx36 clusters on each cone pedicle (Fig. 1F; Fig. 1 – source data 1), along the telodendria
173 and over the upper surface of the cone pedicle.
174
175 **Blue cones – confocal microscopy**
176
177 Blue cones initiate a specific color-coded pathway in the mammalian retina (Behrens et al., 2016;
178 Dacey and Lee, 1994; Haverkamp et al., 2005; Kouyama and Marshak, 1992). Blue cones in the
179 dorsal retina were stained in their entirety by use of a blue cone opsin Venus transgenic mouse
180 line (Fig.1, suppl. 1). Alternatively, blue cones were identified using an antibody to blue cone
181 opsin to stain the outer segment and then following the cone arrestin labelled axon down to the
182 pedicle in a confocal series (Fig.1, suppl. 2, Video 3). In either case, a sparse mosaic of "true
183 blue" cones were located in the dorsal retina (Nadal-Nicolás et al., 2020). We find that the
184 pedicles of blue cones have telodendria bearing Cx36 labeled clusters in a manner
185 indistinguishable from green cone pedicles (Fig. 1G; Fig.1, suppl. 2). Thus, it appears that blue
186 cones also make numerous Cx36 gap junctions with rods.
187
188
189 **Cx36 clusters are located on rod spherules, close to the opening of the post- synaptic**
190 **compartment**
191
192 In high-resolution confocal images (63x objective, NA 1.4, Zeiss Airyscan), the Cx36 elements
193 occur exclusively where cone telodendria contact the base of each rod spherule (Fig. 2A). Some
194 rod/cone contacts have multiple Cx36 puncta (arrow, Fig. 2A). In these images, rod spherules

195 appear as oval structures (blue) including two unlabeled compartments or holes, separated by the
196 synaptic ribbon, immunolabeled for ribeye (white in Fig. 2B). The lower hole in the rod
197 spherule of Fig. 2B contains the mGluR6-labeled (green) tips of rod bipolar cell dendrites and
198 was thus identified as the post-synaptic compartment. The upper hole contains a single large
199 mitochondrion, labeled for the mitochondrial translocase TOMM20 (red). To quantitatively
200 determine the position of Cx36 labeled points, we captured vGlut1 labeled rod spherules and
201 generated a mean structure by aligning, stacking and averaging the images from 18 complete rod
202 spherules. The sites of individual Cx36 elements were marked and found to be located around
203 the base of the mean rod spherule (Figs. 2C, 2D). A spline curve was fitted to the outline of the
204 mean rod spherule and, after linearizing this curve, the density of Cx36 was plotted. The twin
205 peaks of the resulting curve show that Cx36 (red) is distributed around the mouth of the synaptic
206 opening, shown by a drop in the vGlut1 labeling (blue) (Fig. 2E). In the same region, the
207 labeling for the cone signal (green) is high suggesting that Cx36 gap junctions occur at
208 telodendrial contact points with rods. Two potential outliers, at approximately 3 o'clock and 9
209 o'clock (Fig. 2C), were actually located on other nearby rod spherules and so were excluded
210 from the analysis. From the mean structure of 18 rod spherules, all Cx36 elements (2.5 $\pm$
211 0.76/rod, (mean $\pm$ SD, n=45) are located at the base of the rod spherule, within 1 - 2μm of the
212 opening to the post synaptic compartment.
213
214 To estimate the fraction of rods that are coupled to cones, we counted the number of Cx36
215 labeled points at the base of each rod spherule where there was contact with a cone, excluding
216 any rod spherules that were not completely contained within the section. From three different
217 samples, 116/116 rod spherules have cone contacts and Cx36 labeling close to the synaptic

218 opening (Jin et al., 2020). Frequently, there are multiple Cx36 labeled points at the base of a
219 single rod spherule; the number of Cx36 elements ranged from 1 - 6 with a mean of 2.4 ± 0.97
220 (mean ± SD, n=116 rods, total 276 Cx36 labeled points) (Fig. 2F, 2G; Fig. 2 – source data 1).
221 Presuming that a Cx36 cluster indicates the presence of a gap junction, we conclude that every
222 rod spherule was coupled to a nearby cone.
223
224
225 **Serial Blockface Electron Microscopy**
226
227 The e2006 SBF-SEM dataset is derived from a block of mouse retina including 164 cone
228 pedicles and thousands of rod spherules with a voxel size of 16.5 x 16.5 x 25 nm (Helmstaedter
229 et al., 2013). Cone pedicles are easily recognized as the largest structures in the OPL and we
230 were able to map them and register the resulting map with the data from Behrens et al (2016)
231 (Fig. 3A). From these data, we could locate the blue cone pedicles previously identified by their
232 selective contacts with blue cone bipolar cells (Behrens et al., 2016). Rod spherules were also
233 easily identified as the numerous round and compact structures with prominent post-synaptic
234 inclusions in the synaptic invagination. In this dataset, rod spherules are 2-3µm in diameter and
235 they are massed above and surrounding the cone pedicles (Fig. 3B), usually oriented with the
236 synaptic invagination at the base.
237
238
239 **Skeletons show Many Contacts between Cone Telodendria and Rod Spherules**
240

241 To assess potential gap junctional contacts between cone pedicles and rod spherules, we chose a
242 patch of 29 adjacent cones to skeletonize, meaning we followed their processes to nearby
243 contacts or termination. This patch included 13 central cone pedicles surrounded by a ring of 16
244 additional cone pedicles (Fig.3A). Some calculations were based on the central 13 cones to
245 avoid edge artefacts. All skeleton data are provided in Fig. 3 – source data 1 and summarized in
246 Table 1, Appendix 2. This area contained one blue cone pedicle but, in addition, we analyzed all
247 the blue cone pedicles in the data set, as identified by Behrens at al (2016) (summarized in Table
248 2, Appendix 2). We also examined several other locations, including areas with a sparse
249 distribution of cone pedicles, to be sure we did not select an atypical area (Fig. 3A, Fig. 4, suppl.
250 1, C & D). The mosaic of cone pedicles with their overlapping telodendria is plotted in Fig. 3C.
251 Cone axons were followed into the ONL and a projection shows that the telodendria are
252 contained within the upper part of the OPL (Fig 3D).
253
254 We started our analysis with a single cone pedicle (cone 5), near the center, which had a complex
255 but typical field of telodendria approximately 10µm in diameter, and we marked the position of
256 every rod spherule in contact with this cone (Fig. 4A). Cone 5 has contacts with 34 rod
257 spherules which included every rod spherule within the telodendrial field. In a projection, it can
258 be seen that the telodendria extend laterally and above the cone pedicle, reaching up to the
259 overlying rod spherules (Fig. 4A). Many, but not all, telodendria terminate at the base of a rod
260 spherule. The skeleton of a blue cone pedicle (cone 2) is similar (Figs. 4A, bottom and 4B,
261 arrow).
262

263 Outlining the telodendrial fields and adding the rest of the cone pedicles shows a dense matrix of
264 overlapping telodendria (Fig. 4B) each with an area of 103 ± 20 μm^2 (mean ± SD, n=29, Fig. 4F;
265 Fig. 4 – source data 1) and a coverage estimated at 1.56 (n=29 cones). Each cone contacts 43 ±
266 5.4 rod spherules (mean ± SD, n=29 cones) (Fig. 4C & G; Fig. 4 – source data 1), including
267 every rod spherule within its field, typically at the base. Plotting convergence (number of rod
268 spherule contacts per cone) against the pedicle area shows a slight trend for the largest cone
269 pedicles to contact more rods spherules (Fig. 4H; Fig. 4 – source data 1).
270
271 Examining these contacts from the perspective of the rod spherules, we coded the overlying rod
272 spherules in the same color as each cone pedicle. Rod spherules with contacts from two or three
273 of the central 13 cone pedicles are marked black or dark grey respectively with non-contacted
274 rod spherules marked as light grey. Viewing the resulting map quickly makes the point that most
275 rods are contacted by two or three cone pedicles (Figs. 4C; Fig. 4, suppl. 1A). Omitting the cone
276 pedicles (except for one example) and all rod spherules in contact with those cones, leaves only
277 an annulus of rod spherules outside the field of reconstructed cones and demonstrates the almost
278 total absence of rods with no cone contacts (Fig. 4, suppl. 1, B). We found 3/811 (0.4%) rods
279 without cone contacts within the field of 29 cones, an insignificant fraction. As a precaution, we
280 also checked a sparse patch with a rare hole in the cone mosaic (Fig 4. Suppl. 1, C and D). Even
281 here, more than 95% of rods received cone contacts.
282
283 If each cone contacts every rod spherule within its telodendrial field, then in areas where the
284 cone telodendria overlap, each rod must receive contacts from multiple cones. This is clearly the
285 case, and, in fact, most rods receive contacts from two, three or, rarely, four cones. A simplified

286 map for two adjacent cones is shown in Fig. 4D, while the contact map for all 29 cones is shown
287 in Fig. 4 supplement 2A. Of approximately 40 rods in contact with each cone pedicle, only a
288 few have exclusive contacts with a single cone (7.2 $\pm$ 3.4, mean $\pm$ SD, n=13 central cone
289 pedicles). Most rods receive contacts from several cone pedicles while adjacent cone pedicles
290 share as many as 23 rod spherules, (mean $\pm$ SD = 6.2$\pm$4.7, n=79 cone pairs) (Fig. 4 suppl. 2B;
291 Fig. 4 – source data 2). There is a pronounced edge effect because the outermost ring of cone
292 pedicles lacks the overlap from further unanalyzed cones: to avoid this, we analyzed the rod
293 contacts of the central 13 cone pedicles. In this area, rods with multiple cone contacts were the
294 norm; 74% of rod spherules received contacts from two or three cones, yielding a rod to cone
295 divergence of 1.9. (Fig. 4E). This reflects the density of the telodendrial network and the large
296 number of rod/cone gap junctions in the OPL. Clearly, each rod spherule has the potential to
297 make several contacts with close-by cones, in agreement with the confocal data showing the
298 distribution of Cx36.
299
300
301 **Blue Cone Skeletons**
302
303 The skeleton of a blue cone, defined by its bipolar cell contacts (Behrens et al., 2016; Nadal-
304 Nicolás et al., 2020), is also shown in figure 4A and the analysis of all five blue cones from the
305 dataset of Behrens et al, (2016) is presented for comparison with green cones (Fig. 4F & G). The
306 blue cone data are summarized in Table 2, Appendix 2. The telodendrial area of blue cones may
307 be slightly smaller, 85 $\pm$ 19μm^2 (mean $\pm$ SD, n=5) (Fig. 4F) but the difference is not significant
308 due to the small sample size. By all other measures, blue cones are indistinguishable from green

309 cones. Blue cones contact all rod spherules, (40 ± 5.1, mean ± SD, n=5) within their telodendrial
310 field, most of which also receive contact from adjacent green cones. Thus, there is no evidence
311 for color selective rod contacts.
312
313
314 **Segmentation and Reconstruction**
315
316 We segmented several cone pedicles and the rod spherules contacted by each cone pedicle. The
317 contact sites, where the cell membrane of a cone telodendron merged with the cell membrane of
318 a rod spherule, were highlighted. These contact pads could then be superimposed on either the
319 cone pedicle or the surface of the overlying rod spherules. Typically, the telodendrial contacts,
320 often from more than one cone, appear as arcs, close to the synaptic opening of rod spherules
321 (Fig 5, A-D) (Kolb, 1977; Smith et al., 1986; Tsukamoto et al., 2001). Confocal analysis also
322 demonstrated multiple cone contacts with a single rod spherule (Fig. 5E).
323
324 The reconstruction of adjacent cones 3 & 5 shows a complex field of telodendria extending
325 laterally and upwards (distally) from the pedicles (Fig. 5F). Their telodendria interdigitate,
326 mostly avoiding each other; the sparse cone-to-cone contacts will set a limit on cone/cone
327 coupling. We also reconstructed all the rod spherules in contact with these cones (Fig. 5G,
328 Videos 4 & 5). Most of the overlying rod spherules have telodendrial contacts (Figs 5A & C)
329 but a few make direct contacts with the upper surface or roof of the cone pedicle (Fig. 5B & D,
330 Fig. 5 suppl. 1A). When the contact sites with rods are displayed on the cone pedicles, the
331 appearance is similar to the 3D reconstruction of confocal material showing the distribution of

332 Cx36 clusters on a single cone pedicle (Figs. 1D & 5H). When the contact sites are displayed on
333 the rod spherule lower surfaces, it is obvious that most telodendrial contacts are very close to the
334 mouth of the synaptic invagination, often forming a curved line or horseshoe around it (Fig. 5I,
335 J), within 1-2µm. Neighboring cone pedicles often contact the same rod spherules. At such
336 sites, the contact pads from both cone pedicles can be found, often interspersed around the
337 synaptic mouths of the rod spherule (Fig. 5J & K, Video 4 & 5). The cone contact sites are
338 consistent with the location of Cx36 near the mouth of the synaptic invagination and thus
339 indicate the potential presence of rod/cone gap junctions (Fig. 5E). However, a contact pad may
340 exceed the extent of a gap junction and therefore does not predict its size (see below).
341
342 Of the cone pedicles that were completely reconstructed, cones 5, 3 and 2 (a blue cone), had 57,
343 59 and 54 contact pads respectively. Thus, the number of contact pads is close to the number of
344 Cx36 clusters per cone pedicle, (51 $\pm$ 8.9, mean $\pm$ SD), from the confocal analysis, and this
345 suggests that most of the contact pads include gap junction sites. There were a few examples
346 where a cone telodendron contacts a rod spherule far from the synaptic invagination, often in
347 transit to another location, and these can show large areas of contact. But these sites are not
348 associated with Cx36 labeling in the confocal data. In other words, these are incidental contacts
349 of passage, not gap junctions, and they were excluded from our analysis.
350
351 There are a few anomalies in the OPL: some rod spherules sit directly astride a cone pedicle and
352 receive few or no telodendrial contacts. Instead, they make direct contacts with the roof of the
353 cone pedicle (Fig. 5 suppl. 1). In addition, the lowest (most proximal) row of rods in the ONL
354 do not have axons or spherules (Li et al., 2016). Instead, the synaptic machinery is included in

355 the lowest crescent of the cell body, adjacent to the OPL. These low rods represent the most
356 distal synaptic structures in the OPL, yet they still receive contacts from cone telodendria (Fig. 5
357 suppl. 2). Finally, there are a few rod spherules below (proximal to) the level of the cone
358 pedicles. These are often inverted so the mouth is on top and this is the site of telodendrial
359 contacts (Fig. 5 suppl. 3). Thus, in every case, including these anatomical variations, cone
360 contacts occur close to the rod synaptic opening, coincident with the location of Cx36. These
361 sites very probably contain Cx36 rod/cone gap junctions.
362
363
364 **Blue Cone Segmentation**
365
366 Based on the work of Behrens et al. (2016), who identified the cones in contact with the blue
367 cone bipolar cell (b9), we could locate the blue cones in the map of cone pedicles. The
368 telodendrial field of cone 2, a blue cone, contacts 41 rod spherules and overlaps substantially
369 with the surrounding cones (Fig. 5, suppl.4A). This blue cone pedicle made the same types of
370 rod contacts as other cones, including telodendrial contacts, roof contacts and contacts with the
371 rods in the bottom row of the ONL (Fig. 5, suppl.4B). Reconstructing in 3D shows typical
372 contact pads around the mouth of the overlying rod spherules with alternating contributions from
373 multiple cones, including this blue cone. (Fig. 5, suppl.5). Thus, blue cone pedicles also make
374 rod/cone gap junctions and both blue and green cones can make gap junctions with the same rod.
375 We found no evidence of color-specific coupling.
376
377

378 **SBF-SEM, Singer dataset (eel001)**

379

380 While the SBF-SEM data analyzed above provided extensive information about close
381 appositions between cone pedicles and rod spherules, the sample preparation was not appropriate
382 to resolve definitive gap junctions in the tissue. To demonstrate that the contact pads described
383 above represent the presence of gap junctions, we also examined rod/cone contacts in a SBF-
384 SEM dataset (eel001) in which synapses and rod/cone gap junctions were visible. In Fig. 6 A &
385 B, a roof contact between a cone pedicle and an overlying rod spherule is shown. There is clear
386 separation between the cell membranes until a darkly stained chromophilic area where the
387 membranes merge indicating a gap junction approximately 350nm in length. The post-synaptic
388 inclusions of the rod spherule show that this site is close to the opening of the post-synaptic
389 compartment. We have shown above that Cx36 occurs at such contacts between rods and cones
390 and therefore conclude that this demonstrates the presence of a gap junction.

391

392

393 **FIB-SEM to Visualize Gap Junctions**

394

395 We also obtained two FIB-SEM data sets of mouse OPL (FIB-SEM 1 and FIB-SEM 2) with an
396 isotropic resolution of 4nm, permitting the direct visualization of gap junctions. Contacts from
397 cone telodendria at the base of each rod spherule show darkly stained gap junctions consistent
398 with the location of Cx36 labeling (Fig. 6C, D). It should be noted that the area of telodendrial
399 contact is frequently larger than the size of the gap junction (Fig. 6D). Thus, while contact pads

400 in the SBF-SEM e2006 images indicate the potential for a gap junction (Fig. 5 H-K), they do not
401 predict its size.
402
403 Sometimes, what appear as small separate gap junctions in a single section merge in nearby
404 sections to form one large continuous gap junction. An example is shown in Fig. 6E-H; two
405 small gap junctions on either side of the synaptic opening are part of a horseshoe structure
406 similar in shape to many of the reconstructed contact pads. Reconstructing in 3D, shows one
407 large gap junction encircling the base of the rod spherule with a length of approximately 1.5µm
408 (Fig. 6H, Video 6). This curved structure is highly reminiscent of the curved gap junction strings
409 revealed by freeze-fracture EM (Raviola and Gilula, 1973). In the OPL, a few large gap
410 junctions of a similar shape, >1µm long, were readily apparent in the confocal view of
411 wholemount retina labeled for Cx36 (Jin et al., 2020).
412
413 We were able to rotate these gap junction contacts in 3D and estimate the gap junction size from
414 the en face view, as well as the distance from the mouth of the post-synaptic compartment. We
415 analyzed 42 complete rod spherules with a total of 135 rod/cone gap junctions. These data are
416 summarized in Table 3, Appendix 2. In the two FIB-SEM datasets, 42/42 rod spherules have
417 gap junctions close to the mouth of the synaptic compartment consistent with the location of
418 Cx36 (Figs 2A-E). We could not always trace the contact back due to the small volume of these
419 high-resolution data sets, but when it was possible, in 112 cases, 100% of the gap junction
420 contacts were identified as a cone. The number of gap junctions per rod spherule ranged from 1-
421 6 with a mean of 3.2±1.2, (mean, ± SD, n=135, Fig. 7A; Fig. 7 – source data 1). The mean
422 distance from the synaptic mouth was 0.69 ± 0.64µm, (mean, ± SD, n=135), but this is a skewed

423 distribution. 84% of gap junctions lay within 1µm of the synaptic mouth with a median distance
424 of 0.44µm; 94% were within 2µm (Fig. 7B & C; Fig. 7 – source data 1), coincident with the
425 position of cone contacts and the location of Cx36 labeling (Fig 2C-E). There were 8 gap
426 junctions, 6% of the total, which fell outside this range. When these outliers were traced back,
427 the contacts were identified as cones in every case, so despite their distant location relative to the
428 rod synaptic mouth, they were identified as rod/cone gap junctions.
429
430 The identity of the dense chromophilic material visible in EM pictures of gap junctions is
431 unknown but it may consist of gap junction proteins (connexins) in addition to scaffolding
432 proteins and modulatory subunits that are thought to make up a gap junction complex (Lasseigne
433 et al., 2021; Nagy et al., 2018). Freeze-fracture EM analysis of retinal gap junctions has shown
434 that they exist in several distinct forms, from plaques with a crystalline array to sparse linear
435 forms such as ribbons and strings (Kamasawa et al., 2006). En face, the rod/cone gap junctions
436 had a relatively uniform width (~120nm), suggesting a standardized component with a variable
437 length such as a string, as previously reported in freeze fracture studies of the OPL (Raviola and
438 Gilula, 1973). This is also consistent with the low fluorescent intensity of Cx36 in the OPL
439 compared to the IPL, where gap junctions occur predominantly in the form of bright Cx36
440 clusters representing dense two-dimensional arrays of connexons (Kamasawa et al, 2006).
441
442 The mean length of a rod/cone gap junction was 480nm ± 230nm, (mean ± SD, n= 135, 42 rods,
443 Fig. 7D; Fig. 7 – source data 1). Raviola and Gilula (1973) reported the photoreceptor gap
444 junctions as strings of single particles with a spacing of 10nm. Therefore, the average rod/cone
445 gap junction contains a string of 48 connexons. The total gap junction length per rod spherule

446 was 1.5 µm ± 0.44 µm (mean ± SD, n=42, Fig. 7E; Fig. 7 – source data 1) or 150 channels. The
447 largest individual gap junctions occurred when there was only one gap junction per rod spherule
448 (Fig.7, D, F & G, red points; Fig. 7 – source data 1); these were outliers with a length close to the
449 mean total length and they were visible in confocal images as large curved Cx36 labelled
450 structures (Jin et al., 2020).
451
452 In summary, the quantitative analysis of rod/cone gap junctions from the FIB-SEM data,
453 confirms the presence of gap junctions at the sites identified from the contact analysis of SBF-
454 EM data set e2006 and the confocal analysis of Cx36 labeling. Furthermore, rod/cone gap
455 junctions appear as concentric strings around the post-synaptic opening, as reported in the
456 original freeze fracture data (Raviola and Gilula, 1973; Reale et al., 1978).
457
458 **Cone/cone Gap Junctions were not Detected**
459
460 To evaluate cone/cone coupling, we segmented and partially reconstructed six cone pedicles
461 from dataset FIB-SEM 1. The small size/high resolution of the dataset meant that no cone
462 pedicles were complete. Nevertheless, we found 22 contacts between 6 pairs of cones, 3-4
463 contacts per pair (Fig. 7, suppl.1A). This suggests that a single cone pedicle could make around
464 20 contacts with up to six surrounding pedicles given a telodendrial coverage of 1.5.
465
466 Although we were able to locate cone/cone contacts, they did not have the typical appearance of
467 a gap junction. While the contacts were direct, without intervening glial processes, there was no
468 clear membrane density. When a nearby rod/cone gap junction was contained in the same frame,

469 it was much more densely stained (Fig. 7, suppl.1B). We examined all 22 cone/cone contacts,
470 but we were unable to identify any typical electron-dense gap junctions in this material. This is
471 surprising given previous reports of cone/cone coupling in mammals.
472
473
474 **Exclusion of rod/rod gap junctions.**
475
476 Previous work has reported the presence of rod/rod gap junctions (Tsukamoto et al., 2001).
477 However, in our FIB-SEM sample of 42 reconstructed rod spherules, we were unable to locate
478 any rod/rod gap junctions. The location and packing density of rod spherules means they are
479 often adjacent, but we found there is usually clear separation between their membranes.
480 Occasional small contacts between adjacent rod spherules show no membrane density, in
481 contrast to rod/cone gap junctions (Fig. 7, suppl. 1C), and are often distant from the synaptic
482 opening at the base where most Cx36 is clustered in the confocal data. Thus, our FIB-SEM data
483 does not support the presence of rod/rod coupling in the mouse retina. This is consistent with
484 physiological results that show the lack of direct rod/rod coupling (Jin et al., 2020).

485 **Discussion**

486

487 We report the reconstruction of photoreceptor terminals and the size and distribution of rod/cone
488 gap junctions in the OPL of the mouse retina. Cone telodendria contact all nearby rod spherules
489 at Cx36 clusters, close to the mouth of the synaptic opening. Confocal microscopy showed there
490 were over 50 Cx36 clusters per cone pedicle with a mean of 2-3 per rod spherule.
491 Reconstructing an area of 29 cones and 811 rods by SBF-SEM, revealed that cone pedicles,
492 including true blue cones, contacted a mean of 43 rod spherules, reaching > 99% of rods.
493 Conversely, rod spherules diverge to a mean of 1.9 nearby cones. FIB-SEM, at higher resolution
494 but a smaller volume, confirmed that gap junctions occur at telodendrial contacts with rod
495 spherules. String-like rod/cone gap junctions have a mean length of 480nm with 1.7 gap
496 junctions per rod/cone pair yielding 82 connexons and a theoretical maximum conductance of
497 ~1200pS, based on morphology. Previous paired recordings showed a mean conductance
498 between a rod/cone pair of 300pS (Jin et al., 2020), suggesting ~25% of the gap junction
499 channels are open at rest. Rod cone gap junctions are closed by dopamine agonists reducing the
500 conductance to noise levels (~50pS, ~5% open probability; Jin et al., 2020). But the mean
501 rod/cone conductance is raised to ~1000pS in the presence of a dopamine antagonist (Jin et al.,
502 2020), suggesting that the open probability for channels in a rod/cone gap junction may approach
503 100% and have a dynamic range of ~20. A summary diagram showing various rod/cone gap
504 junctions is shown in figure 8.

505

506

507 **Identification of gap junctions**

508

509 In EM material, gap junctions have been difficult to identify due to their size and orientation;
510 unless a gap junction is fortuitously captured in cross section, the membrane density can be
511 difficult to identify. Ideally, there should be enough resolution to reveal the pentalaminar
512 signature of a gap junction, approximately 10nm across (Marc et al., 2018, 1988). Indeed, some
513 authors advocate resampling at high magnification (0.27nm) with goniometric tilt to optimize
514 visibility (Sigulinsky et al., 2020). However, the time investment makes this impractical for
515 every potential gap junction. In our FIB-SEM material, and appropriately fixed SBF-SEM
516 material, the pentalaminar structure of gap junctions cannot be resolved but an area of increased
517 membrane density and chromophilic staining is present where the membranes of a cone
518 telodendron and a rod spherule merge. The identity of the chromophilic material is unknown but
519 presumably it represents the aggregation of connexons and auxiliary proteins at gap junction
520 sites (Lasseigne et al., 2021; Nagy et al., 2018). For rod spherules, this coincides with the
521 location of Cx36 labeling, close to the mouth of the synaptic opening, and so there is a high
522 probability that these sites represent gap junctions.

523

524

525 **Rod/cone Gap Junctions Predominate**

526

527 Our results confirm the original work from cat retina which showed 48 rod contacts per cone
528 with a divergence of one rod to two cones (Smith et al., 1986), very close to the numbers
529 reported here. In the primate retina, freeze fracture EM showed string-like gap junctions of 400-
530 600 nm in concentric arcs around the rod spherule synaptic opening (Raviola and Gilula, 1973).

531 The telodendrial contacts described here, have the same curved appearance and coincide with the
532 location of Cx36 on the lower or vitreal surface of each rod spherule. With FIB-SEM, we found
533 string-like rod/cone gap junctions with a mean length of 480nm, a remarkable tribute to the
534 freeze fracture EM work from nearly 50 years ago. Since that time, Cx36 has been identified as
535 the major neuronal connexin and we show that Cx36 labeling signposts rod/cone gap junctions at
536 the confocal level. In summary, the results from mouse, cat, primate and human retinas all
537 indicate that rod/cone gap junctions are a common feature of the mammalian retina (Kántor et
538 al., 2016; O'Brien et al., 2012; Raviola and Gilula, 1973; Smith et al., 1986).
539
540 The location of most Cx36 clusters at cone contacts with the base of each rod spherule is
541 consistent with previous EM work showing that gap junctions occur at these sites. In fact, they
542 are quite numerous in this study, with a range of 1-6 Cx36 contacts per rod spherule, comparable
543 with 4-6 cone contacts per rod in the cat retina, forming a ring of contacts around the post-
544 synaptic opening of the rod spherule (Smith et al., 1986). In rod spherules from the mouse
545 retina, two gap junction contacts were described, usually on opposite sides of the synaptic
546 opening, mostly arising from a single cone (Tsukamoto et al., 2001). The detailed
547 reconstructions presented here show a mean of 2.4 (confocal) – 3.2 (FIB-SEM) gap junction
548 contacts per rod spherule and the norm is connections with 1-3 different cones. Our results
549 demonstrate that rod/cone gap junctions account for nearly all gap junctions between
550 photoreceptors.
551
552 Previously, some Cx36-GFP labeling was also found in the outer nuclear layer (ONL)
553 (Feigenspan et al., 2004), suggesting that some coupling may occur between somas and/or

554 passing axons. However, we did not observe this pattern with Cx36 antibodies and, in our hands,
555 Cx36 labeling of photoreceptors was restricted to the OPL (Fig. 1). It is possible that the Cx36-
556 GFP construct caused a trafficking defect.
557
558 Rod/cone coupling forms the entry to the secondary rod pathway (Kolb, 1977; Smith et al, 1986).
559 It was previously thought that these gap junctions must be closed at night to preserve the
560 amplitude of single photon responses of individual rods, which underlie scotopic sensitivity
561 (Smith et al., 1986). However, recent work indicates that rod/cone coupling is high at night and
562 low in daytime, due to circadian activity and the influence of dopamine (Jin et al., 2016, 2020).
563 Thus, we have suggested that noise reduction, a consequence of coupling in the photoreceptor
564 network, is a major function of rod/cone gap junctions, in addition to driving the secondary rod
565 pathway (Field et al., 2019; Jin et al., 2020).
566
567
568 **Rods and cones both express Cx36**
569
570 The small number of Cx36 clusters per rod, compared to more than 50 per cone pedicle, a ratio
571 of approximately 20, may explain early failures to detect rod Cx36 (Bolte et al., 2016;
572 Feigenspan et al., 2004). However, there is strong physiological evidence that Cx36 is required
573 for rod/cone coupling (Asteriti et al., 2017; Ingram et al., 2019; Jin et al., 2020) Cx36 is the
574 most common neuronal connexin but it does not pair with other connexins, making only
575 homotypic gap junctions (Koval et al., 2014; Nagy et al., 2018; Teubner et al., 2000). We have
576 recently shown that both rods and cones express Cx36 and that no other connexins are present in

577 either rod or cones (Jin et al., 2020). In addition, Cx36 is required on both sides to form a
578 rod/cone gap junction (Jin et al., 2020; Miller et al., 2017). Thus, the simplest case holds, that
579 both rods and cones express Cx36 and rod/cone gap junctions are heterologous but homotypic
580 (meaning between different cell types but both expressing the same connexons).
581
582
583 **Blue cones are also coupled to rods.**
584
585 Blue cones, identified in confocal work by the presence of S-cone opsin, and in SBF-SEM by
586 their connections with blue cone bipolar cells (Behrens et al., 2016; Nadal-Nicolás et al., 2020),
587 also made telodendrial contacts at Cx36 clusters with all nearby rod spherules (Fig. 4). In the
588 cone networks of primate and ground squirrel retina, there is evidence that blue cones are not
589 coupled to neighboring red/green or green cones (Hornstein et al., 2004; Li and DeVries, 2004;
590 O'Brien et al., 2012), perhaps to maintain spectral discrimination (Hsu et al., 2000). However,
591 we find no evidence for color specificity in rod/cone coupling. In fact, a single rod spherule may
592 be coupled to both blue and green cones (Fig. 5, supplement 5). Thus, rod input to blue cone
593 bipolar cells and downstream circuits is predicted via the secondary rod pathway, in addition to
594 the previously reported primary rod pathway inputs from AII amacrine cells to blue cone bipolar
595 cells (Field et al., 2009; Whitaker et al., 2021)
596
597
598 **Cx36 numbers for rods and cones are consistent**
599

600 We have gathered data for both rods and cones independently. Because they are linked by
601 rod/cone gap junctions, a book-keeping exercise should serve as a check on the data. From
602 individual EGFP-labeled cone pedicles, we estimate that each cone pedicle has 51 $\pm$ 8.9 (mean $\pm$
603 SD, n=18) Cx36 clusters, presumed to represent gap junctions, with nearby rod spherules. From
604 the rod perspective, 43 rods contact each cone with 2.4 Cx36 clusters per rod. But some of these
605 potential gap junctions are made with neighboring cones. To correct for this, we divide by the
606 rod divergence, 1.9. Thus 43 x 2.4/1.9 = 54, the number of Cx36 clusters at rod contacts with a
607 single cone pedicle. This is in close agreement with the number of Cx36 gap junctions counted
608 in confocal reconstructions of individual cone pedicles. These numbers are also close to
609 previous calculations of ~45 Cx36 clusters/cone pedicle, based on the density of Cx36 puncta
610 and the number of cone pedicles from wholemount retina (Jin et al., 2020).
611
612 We calculated the number of gap junctions per rod by two methods, a confocal analysis of Cx36
613 labeled points, and using the FIB-SEM data. Analyzing the FIB-SEM data gave 3.2 gap
614 junctions per rod spherule. In the confocal analysis of Cx36 elements, there were 2.4 gap
615 junctions per rod spherule, 25% less. While these numbers are similar, the EM data gives a
616 higher value. This might be expected because small elements could be missed and two close
617 together could merge and be counted as one in the lower resolution confocal data (Sigulinsky et
618 al., 2020). Clearly, the smallest Cx36 elements may be less than the confocal detection limit,
619 (different from the resolution limit), but these data suggest that we accounted for at least 75% of
620 the photoreceptor gap junctions by confocal microscopy.
621
622

623 **Cone/Cone Contacts were not Detected**

624

625 We were unable to confirm the presence of cone/cone gap junctions in the mouse retina, despite
626 locating more than 20 examples of cone/cone contacts. In each case, there was no indication of
627 the typical membrane density or chromophilic staining at cone/cone contacts. Nearby rod/cone
628 contacts provided prominent control gap junctions for comparison (Fig. 7 suppl. 1B). This result
629 is surprising, given previous reports of cone/cone coupling in several mammalian species,
630 including mouse (DeVries et al., 2002; Kolb, 1977; Smith et al., 1986; Tsukamoto et al., 2001).
631 However, close contacts without gap junctions are not unprecedented. In rabbit retina, many
632 bipolar cells are coupled by gap junctions, but some are not, despite contacts and the presence of
633 gap junctions elsewhere in the same cell (Sigulinsky et al., 2020). Gap junctions do not
634 determine the specificity of neuronal connections.

635

636 However, electrophysiological studies suggest there is weak cone to cone coupling in the mouse
637 retina, which may indicate that cone/cone gap junctions are smaller than rod/cone gap junctions.
638 Cone/cone coupling persists in the rod-specific Cx36 KO, suggesting it is direct (Jin et al., 2020).
639 In the rod Cx36 KO, which should reveal cone/cone coupling, there was some residual Cx36
640 labeling, associated with cone telodendria, which was significantly different from the
641 background noise and may represent a small amount of cone/cone coupling, estimated as 2 gap
642 junctions/cone (Jin et al., 2020).

643

644 Cone to cone coupling has been reported in other mammals but there may be species variation.
645 In the ground squirrel, a cone dominated retina, the low number of rods with the resulting

646 adjacency of the cones may promote cone/cone coupling (DeVries et al., 2002; Li, 2020; Li et
647 al., 2010). In the central primate retina, cones are densely packed and often adjacent, which is
648 not the case in mouse retina. In peripheral primate retina, cones are more widely spaced, and
649 they are connected by a sparse array of telodendria, which seem to target neighboring cones
650 making the pattern of Cx36 labelled gap junctions very obvious, in addition to numerous
651 rod/cone gap junctions (O'Brien et al., 2012). Finally, in the rod-less, cone-only mouse, there is
652 a large increase in Cx36 labeling in the OPL suggesting that cone/cone coupling occurs, at least
653 under these circumstances (Dang et al., 2004). The evidence for photoreceptor coupling,
654 including weak cone/cone coupling, is summarized in Appendix 1.
655
656
657 **No rod/rod gap junctions**
658
659 Previous work in the mouse retina has suggested that rods form a coupled network based on the
660 presence of small rod/rod gap junctions (Tsukamoto et al., 2001). Most of the rod spherules
661 were reported to make gap junction contacts which were characterized as small and with no
662 membrane density (Tsukamoto et al., 2001). Furthermore, some of the rod/rod contact sites were
663 between the spherules and passing rod axons, a location where there is no Cx36 labeling.
664
665 We have searched diligently for rod/rod gap junctions, but we have been unable to confirm their
666 presence. Not only is Cx36 labeling restricted to the base of the rod spherule, around the
667 synaptic opening, but, in the FIB-SEM material, this was almost the only location where we
668 found gap junctions. We mapped the gap junctions from 42 rod spherules and their distribution

669 was in close agreement with the distribution of Cx36 labeling and cone telodendrial contacts.
670 We could not trace every process making a gap junction contact but in 112/112 cases, we could
671 identify the process as a cone telodendron. Even the small number of outlying gap junctions
672 distant from the synaptic opening were traced to cones.
673
674 We did find small contacts between adjacent rod spherules (Fig. 7, suppl. 1C) but there was no
675 membrane density indicating the presence of a gap junction and, in this equatorial position,
676 around the midline where the rod spherules are closely packed, there was no Cx36. We are
677 aware of the difficulty in proving the absence of a particular structure but, based on the evidence
678 presented here, we conclude that there are no rod/rod gap junctions in the mouse retina and this
679 may be a common feature of the mammalian retina.
680
681 In support of this conclusion, apparent rod/rod coupling was eliminated in the cone-specific
682 Cx36 KO, indicating that physiological evidence of rod/rod coupling in wild type retina is
683 actually due to indirect rod/cone/rod coupling via the network (Jin et al., 2020). In the cone-
684 specific Cx36 KO, which should reveal rod/rod coupling, Cx36 labeling of photoreceptors was
685 essentially eliminated, providing no evidence for residual rod/rod coupling (Jin et al., 2020). The
686 rod-specific Cx36 KO produced a similar result but a few remaining Cx36 clusters were
687 attributed to cone/cone coupling. The loss of most Cx36 coupling in either the rod- or cone-
688 specific KO indicates that rod/cone coupling accounts for the majority of photoreceptor gap
689 junctions and provides no support for direct rod/rod coupling. We must emphasize that the
690 weight of the available evidence suggests that there is no rod/rod coupling in the mouse retina.

691 The comparative evidence for photoreceptor coupling, including the lack of rod/rod coupling, is
692 summarized in Appendix 1.
693
694
695 **Calculations of Size and Open Probability for Rod/Cone Gap Junctions**
696
697 Gap junctions are common building blocks of neural circuits throughout the CNS, but there is
698 much that we do not know. For example, in most cases, we do not know their size, the number
699 of connexon channels, their conductance, and perhaps most importantly, their dynamic range or
700 plasticity. The size of the conductance through a gap junction depends not only on the number
701 of connexons and the unitary conductance, but also on the channel activity, usually characterized
702 as the open probability. These are the fundamental properties required to understand the function
703 of gap junctions in neuronal microcircuits. Here, we have an opportunity to estimate these
704 variables.
705
706 There is great variability in gap junction morphology, from strings to crystalline plaques
707 (Kamasawa et al., 2006). Rod/cone gap junctions appear as low-density strings of single
708 particles in freeze fracture EM (Raviola and Gilula, 1973; Reale et al., 1978) and this is
709 consistent with the uniform width of rod/cone gap junctions from our 3D-EM reconstructions, as
710 well as the low intensity of Cx36 labeling compared to the plaque type gap junctions of the inner
711 retina (Kamasawa et al., 2006).
712

713 We calculated the number of connexon channels from the mean length of an FIB-SEM gap
714 junction ~ 480nm, yielding 48 channels per rod/cone gap junction, based on the 10nm spacing of
715 connexons in a string (Kamasawa et al., 2006; Szoboszlay et al., 2016), in close agreement with
716 40-50 particles/string in freeze fracture (Raviola and Gilula, 1973). We estimate there are 3.2
717 gap junctions per rod, but these are shared with several nearby cones. Dividing by the rod to
718 cone divergence (the number of cones contacted by each rod), 1.9, gives 1.7 gap junctions or a
719 mean of 82 connexons between an average rod/cone pair. For a unitary conductance of 15 pS
720 per Cx36 channel (Srinivas et al., 1999), we can calculate the mean maximal conductance
721 between a rod and a cone as ~ 1,200 pS (82 connexons x 15 pS/connexon). It is important to
722 note that this theoretical maximum, if all gap junction channels between a rod/cone pair are in an
723 open state, was derived from our morphological data.
724
725 Using this detailed structural information, combined with our previous conductance
726 measurements from rod/cone paired recordings, we can calculate the properties of rod/cone gap
727 junctions. Our recently published work shows a resting value ~ 300 pS for the rod/cone
728 transjunctional conductance (Jin et al., 2020). Compared to the theoretical maximum above, this
729 indicates a resting open probability of 25%. Notably, this is much higher than previous estimates
730 of around 1% (Connors, 2017; Marandykina et al., 2013). But these earlier values may be low
731 because the size of the gap junctions was estimated by immunofluorescence, which provides a
732 high number for gap junction area and connexon number, with a correspondingly low number for
733 the open probability (Kamasawa et al., 2006; Szoboszlay et al., 2016). More recently, when the
734 number of connexons was accurately measured by freeze fracture EM, the open probability of

735 cerebellar gap junctions was calculated as 18% (Szoboszlay et al., 2016), close to the value
736 derived here.
737
738
739 **Dynamic Range of Rod/Cone Gap Junctions**
740
741 Rod/cone coupling is modulated by dopamine (Ribelayga et al., 2008; Jin et al., 2020). In our
742 previous studies, we showed that the dynamic range of rod/cone coupling, driven by D2
743 dopaminergic agonists and antagonists, varied from a noise level ~50pS in the closed state to a
744 mean maximum of 1070pS (Jin et al., 2020). Compared to the theoretical maximum above,
745 these values translate to a minimum open probability of 4% and a maximum of 89% of available
746 Cx36 channels. This is a very surprising result because previous measures of open probability
747 have produced such low estimates (Connors, 2017), but we believe it is consistent with our data.
748 For the first time, it suggests that the range of gap junctions can be modulated from close to 0 to
749 nearly 100% of available Cx36 channels. In other words, all of the channels in these small
750 rod/cone gap junctions are switchable and may contribute to their plasticity.
751
752 The diffusion coefficient through Cx36 gap junctions, a proxy for conductance, was correlated
753 with the phosphorylation of Cx36 as measured using phospho-Cx36 antibodies (Kothmann et al.,
754 2009; O'Brien, 2014). Pharmacological manipulation using dopamine agonists or antagonists
755 produced phosphorylation-driven changes in tracer coupling that encompassed a 20-fold range of
756 diffusion coefficients, producing a large dynamic range for gap junction plasticity. In the present
757 experiments, the ratio of minimum to maximum open channels, from 4% - 89% or 50-1000pS,

758 was also approximately 20. This is very similar to the dynamic range derived from tracer
759 coupling studies with phospho-specific Cx36 antibodies. While these calculations are
760 necessarily approximate, they support the concept that gap junctions provide a versatile
761 component, offering a large range of plasticity in neural circuits. In the retina, rod/cone coupling
762 may reduce transduction noise in the photoreceptor network and the modulation of rod/cone gap
763 junctions also provides a switchable entry to the secondary rod pathway, which varies with light
764 intensity and/or the circadian cycle (Bloomfield and Völgyi, 2009; Field et al., 2019; Jin et al.,
765 2020; Jin and Ribelayga, 2016).

766 # Methods

767

768 **Animals**

769

770 All animal procedures were reviewed and approved by the Animal Welfare Committee at the
771 University of Texas Health Science Center at Houston or by our collaborators' local Institutional
772 Animal Care and Use Committees. C57BL/6J (stock no. 000664) mice were purchased from the
773 Jackson laboratories. We used mice 2 to 6 months of age of either sex. Animals were housed
774 under standard laboratory conditions, including a 12-hour light/12-hour dark cycle.

775

776

777 **Antibodies and immunocytochemistry.**

778

779 Mice were anesthetized by intraperitoneal injection of a ketamine/xylazine mix solution (100/10
780 mg/kg) before being euthanized by cervical dislocation. Eyes were rapidly collected,
781 hemisected, the vitreous was removed and the resulting eyecup was placed in 4%
782 paraformaldehyde in phosphate-buffered saline (PBS) at room temperature for 1 to 2 hours.
783 Vibratome sections (Leica VT 1000S) or whole-mounted retinas were reacted with a cocktail of
784 antibodies (Table 1), according to procedures described previously (Li et al., 2013; O'Brien et
785 al., 2012). Briefly, sections were washed and blocked in 3% donkey serum/0.3% Triton X-100
786 (in PBS) for 2 hours (overnight for whole mounts) and incubated overnight at room temperature
787 with a cocktail of primary antibody(ies) in 1% donkey serum/0.3% Triton X-100 (in PBS) (7
788 days for whole mounts). Tissues were processed free-floating on an oscillating platform at 1Hz.

789 Following incubation with the primary antibody, sections were rinsed in PBS (6×, 20 min) and
790 reacted with a secondary antibody(ies) for 2 hours (overnight for whole mounts) at room
791 temperature in the dark. Donkey Alexa Fluor–, Cy3-, or DyLight-conjugated secondary
792 antibodies were purchased from Jackson ImmunoResearch Laboratories Inc. (West Grove, PA)
793 and used at 1:600 dilution. Last, sections or whole mounts were covered with mounting medium
794 and sealed with nail polish. DAPI (4′,6-diamidino-2-phenylindole) (100 μg/ml) was added to the
795 mounting medium to stain the nuclei.
796
797
798 **Blue cone opsin-Venus mouse line**
799
800 A bacteria artificial chromosome (BAC) clone (bMQ-440P15) from a SV129 genomic library
801 (bMQ), encompassing the entire mouse Opn1sw locus, was used to create the Opn1sw_Venus
802 BAC transgenic construct through ET recombination as described elsewhere (PMID: 9771703).
803 Briefly, a Venus-bGH PolyA-NeoR (flanked by FRT sites) cassette was integrated into the
804 Opn1sw locus on the BAC clone replacing coding region of exon 1 to generate the Venus-bGH-
805 Neo knockin version of the BAC clone. Recombination was verified by PCR reactions
806 specifically designed to detect recombination junctions by ET recombination (or homologous
807 recombination). This BAC clone carrying the reporter cassette was further trimmed, through ET
808 recombination, to retain a 15 kb fragment including upstream regulatory sequence (10kb
809 upstream of the coding region), the KI cassette and the ~2 kb sequence downstream of exon 2 of
810 the Opn1sw gene. The intended transgenic construct was verified by overlapping PCR and
811 Sanger sequencing. Transgenic F0 founders were created by microinjecting the transgenic

812 construct (1ng/µl) into fertilized eggs from C57bl6/j donors followed by genomic PCR screening
813 amplifying the reporter insert.
814
815
816 **Confocal Microscopy Image Acquisition**
817
818 A Zeiss LSM-800 confocal microscope with Airyscan was used for 4 channel imaging of retinal
819 whole mounts and sections with a 63x (N.A. 1.4) oil-immersion objectives. Images with 30 - 40
820 nm pixel size were acquired in series of 0.15 µm optical sections. Airyscan images were
821 processed by Zen software (Zeiss) to yield super-resolution images. We measured the full width
822 at half maximum of the point spread function for this instrument as 170nm using 0.1 µm latex
823 beads (Molecular Probes). Figures were presented as short stacks of 2 - 6 images. Images were
824 processed in ImageJ, Imaris (Oxford Instruments) or Photoshop (Adobe Systems Inc) for
825 contrast enhancement and further analysis.
826
827
828 **Quantitative Analysis of Cx36 clusters**
829
830 Single cones: retinal sections from OPN4-EGFP mice were used because only a few cones were
831 EGFP positive and it was possible to image well-isolated single cone pedicles. Airyscan images
832 were loaded in Imaris software and the colocalization between the cone (EGFP) and Cx36 (Cy3)
833 was analyzed. Neighboring colocalized voxels were grouped as a 3D object by surface rendering
834 and the number of extracted 3D objects was measured.

835

836 Rod spherules: an antibody against the synaptic vesicular glutamate transporter (vGlut1) was
837 used to label rod spherules. It does not stain the cell membrane and thus underfills rod spherules
838 (Quraishi et al., 2007). Some sections were also stained for Plasma Membrane Calcium ATPase
839 (PMCA) which stains the rod spherule membrane (Johnson et al., 2007), encircling the vGlut1
840 labeling (Fig. 5, suppl. 3A). Due to lack of clear colocalization between Cx36 and the rod
841 marker (vGlut1), the number of Cx36 clusters per rod was counted manually. Some rod
842 spherules were excluded from analysis if they were too close to link a Cx36 cluster to a specific
843 rod. A total of 116 well-isolated rod spherules in 3 retinal sections were chosen to analyze for
844 the number of Cx36 clusters. To analyze the position, a mini-stack of 6 x 0.15µm optical
845 sections from 18 rod spherules were extracted, aligned and averaged (ImageJ). A spline curve 8
846 pixels (272nm) wide was applied to the perimeter and the intensity profile for Cx36 was plotted
847 linearly around the synaptic opening.

848

849

850 **Connectivity analysis, SBF-SEM (e2006)**

851

852 A region in the OPL from a publicly available serial block-face scanning EM (SBF-SEM) dataset
853 e2006, voxel size 16.5 x 16.5 x 25 nm, (Behrens et al., 2016; Helmstaedter et al., 2013),
854 including 164 cone pedicles was analyzed using KNOSSOS software (Helmstaedter et al., 2011)
855 (https://knossos.app/). A volume of approximately 15 µm (OPL depth) × 50 µm × 50 µm in the
856 OPL was chosen to analyze, in which we identified 29 cone pedicles and 811 rod spherules.
857 Because there are some areas of relatively low cone density, an additional area including 6

858 widely spaced cone pedicles was also analyzed. The whole e2006 dataset included a total of 6
859 blue cones (Behrens et al., 2016) but one was located at the edge of the dataset and was
860 truncated. Thus, a total of 5 blue cones were analyzed.
861
862 Skeletons: we traced the telodendria from all 29 cone pedicles by skeletonization with
863 KNOSSOS. All rod spherules contacted by a specific cone were identified. We used the
864 membrane fusion between cone pedicle/telodendria and rod spherule to indicate rod/cone
865 contact. The contact information was stored as an annotation directory in KNOSSOS and further
866 analyzed using Excel (Microsoft) and Origin (OriginLab Corp).
867
868 Segmentation and 3D reconstruction: A volume of 27 μm (OPL plus a part of ONL) × 27 μm ×
869 39 μm was extracted from the e2006 dataset to segment using Microscopy Image Browser
870 (Belevich et al., 2016). The segmented voxel data were loaded into Imaris to create a 3D
871 reconstruction by surface rendering. Images were constructed in Imaris by rotating and adjusting
872 transparency as required.
873
874
875 **SBF-SEM, Singer dataset** (eel001)
876
877 An excised retina was fixed for one hour at room temperature with 2% glutaraldehyde in 0.15 M
878 cacodylate buffer, washed in three changes of the same buffer, and postfixed with 1% osmium
879 tetroxide in 0.15 M cacodylate containing 1.5% potassium ferrocyanide. A wash in three changes
880 of distilled water followed the reduced osmium fixation and preceded an en bloc fix in 2%

881 aqueous uranyl acetate. Dehydration in a graded series of ethanol (35% to 100%) and infiltration
882 in a propylene oxide:epoxy resin series was followed by embedding and polymerization in epoxy
883 resin. Imaging by SBF-SEM was performed under contract with Renovo Neural (Cleveland, OH)
884 using a FEI Teneo Volume Scope. Beam current was 50 pA and the face was imaged with 7 x 7
885 x 40 nm resolution. Each face image spanned the width of the retina from the first layer of
886 photoreceptor cell bodies in the ONL to the ganglion cell bodies in the GCL and comprised two
887 stitched fields of 8192 x 8192 pixels for a dimension of 8192 x 16384 pixels or 57.34 x ~114.68
888 µm. 1649 slices in total were acquired, making the z-depth traversed = 65.96 µm. Image stacks
889 were viewed using Knossos and processed in Photoshop.
890
891
892 **FIB-SEM sample preparation**
893
894 Mice were euthanized and enucleated; retinas were quickly dissected and placed in 3%
895 paraformaldehyde and 1% glutaraldehyde for 30 minutes, then processed for electron
896 microscopy using the Dresden protocol (Paridaen et al., 2013). The resulting resin blocks were
897 trimmed to contain the OPL within 25µm of the top-edge of the block, cut and mounted to a 45°
898 pre-tilted stub, and coated with 8nm of carbon. Three-dimensional data were acquired using the
899 Helios G3 NanoLab DualBeam FIB-SEM. In brief, a focused beam of gallium atoms ablated
900 4nm off the surface of the sample (FIB conditions: 30keV accelerating voltage, 790pA beam
901 current), comprising the scanning electron microscope (SEM) imaging area, with a field of view
902 around 25µm. The freshly ablated surface was then imaged by backscattered electrons using the
903 In-Column Detector (SEM conditions: 400 pA beam current, 3KeV accelerating voltage, 4nm

904 per pixel, and 3µs dwell time; image resolution: 6144 x 4086, 4nm isotropic). Around 1,149
905 (FIB-SEM 1 dataset; 1,342 for FIB-SEM 2 dataset) ablation and imaging cycles were run over a
906 three day period, resulting in a sample depth of roughly 4.6µm. Images were then registered
907 using the Linear Stack Alignment with SIFT algorithm (Fiji) and cropped to remove artifacts
908 arising from the alignment.
909
910
911 **Gap junction position and size analysis from FIB SEM**
912
913 Individual rod spherules were cropped from the datasets and segmented for 3D reconstruction as
914 described above for the e2006 dataset. Gap junctions were identified by a darkly stained area of
915 merged membranes. The distance from a gap junction to the synaptic opening of a rod spherule
916 was calculated using the oblique slicer tool in Imaris to align the center of the mitochondria and
917 the postsynaptic opening in a single plane. Gap junction length was visualized using the oblique
918 slicer to create an en face view. Some gap junctions showed belt-like structures with curvature
919 and torsion. Due to the complexity of the structure, the size of these gap junctions was estimated
920 as a simplified rectangular shape by measuring the length and average width of the belt. The
921 acquired data were analyzed in Excel and Origin.

922 **Table 1: Antibodies**

923

Antibody	Source	Catalog #	Species	Dilution	Notes
Cone Arrestin	Millipore	AB15282	rabbit	1:1000	Labels cones, including pedicle
Cx36	Millipore	MAB3045	mouse	1:1000	Cx36 gap junctions
vGlut1	Synaptic Systems	135304	guinea pig	1:3000	Labels PR terminals, esp. rod spherules
Blue cone opsin	Millipore	AB5407	rabbit	1:1000	Blue cone outer segments
Ribeye/CtBP2	BD Transduction	612044	mouse	1:500	Synaptic ribbon marker
TOMM20	Sigma-Aldrich	HPA011562	rabbit	1:1000	Mitochondrial marker
mGluR6	Generous gift from Kiril Martemyanov		sheep	1:1000	mGluR6 receptors of ON bipolar cells and rod bipolar cells
PMCA	Santa Cruz Biotechology	sc-28765	rabbit	1:200	Labels rod spherule plasma membrane

924

925 **Appendix 1 –**

926

927 **Comparison of Photoreceptor Gap Junctions**

928

929 For comparison, we have summarized the evidence for rod/cone, cone/cone, and rod/rod gap
930 junctions in the mouse retina.

931

932

933 **Rod/cone**

934

935 1. Cones contact all rods.
936 2. Cx36 labeling at the base of each rod spherule; no other connexins expressed by
937 photoreceptors (Jin et al., 2020).
938 3. Cx36 labeling dramatically reduced in either rod or cone specific Cx36 XOs, consistent with
939 the predominance of rod/cone gap junctions and the requirement for Cx36 on both sides of a
940 rod/cone gap junction (Jin et al., 2020).
941 4. FIB-SEM shows gap junctions at the base of each rod spherule, coincident with cone
942 contacts and Cx36 immunoreactivity.
943 5. Paired recordings show a large conductance between rod/cone pairs (resting state, dark-
944 adapted), mean 300pS (Jin et al., 2020).
945 6. Rod/cone coupling abolished in either the rod- or cone-specific Cx36 XO (Jin et al., 2020).
946 7. Rod signals transmitted to cones via rod/cone gap junctions (Jin et al., 2020).

8. Rod/cone gap junctions are common in several mammalian species (Smith et al, 1986; O'Brien et al., 2012).

We conclude all rods are coupled to cones.

Cone/cone

1. Some cone/cone contacts, mostly between telodendria.
2. While Cx36 is colocalized with the cone telodendrial network, most Cx36 clusters are rod/cone GJs. We were unable to identify cone/cone Cx36 clusters in the mouse retina.
3. FIB-SEM shows some contacts between adjacent cones but no membrane density at contact points.
4. Paired recordings show weak cone/cone coupling, a fraction of rod/cone coupling, ~60pS in mouse (Jin et al., 2020), but ~250pS in ground squirrel where Cx36 between cones is prominent (DeVries et al., 2002).
5. Cone/cone coupling was preserved in the rod Cx36 XO, suggesting cone/cone coupling is direct.
6. In the rod XO, which should reveal cone/cone coupling, a few Cx36 clusters left, significantly different from cone Cx36 XO or pan Cx36 XO, (Jin et al., 2020).
7. Cone/cone coupling reported in other species, such as ground squirrel and primate,
8. In the rod-less, cone-only mouse, there is a large increase in Cx36 labeling in the OPL (Dang et al., 2004).

970

971 The evidence for cone/cone coupling is weak for the mouse retina. Despite the fact that we were
972 unable to identify cone/cone gap junctions, there is physiological evidence for weak cone/cone
973 coupling (Jin et al., 2020). While the presence of cone/cone coupling in the mouse is equivocal,
974 there is strong evidence for cone/cone coupling in other species such as primate and ground
975 squirrel. (DeVries et al., 2002; O'Brien et al., 2012).

976

977

978 **Rod/rod**

979

980 1. Few rod/rod contacts despite spherule packing in the OPL
981 2. No Cx36 labeling at rod/rod contacts
982 3. In the cone-specific Cx36 XO, which should reveal rod/rod coupling, there was no remaining
983 Cx36 labeling in the OPL above a very low background (Jin et al., 2020).
984 4. FIB-SEM of rod/rod contacts shows no dense staining typical of a gap junction
985 5. Paired recordings show apparent rod/rod coupling was abolished in the cone Cx36 XO,
986 indicating indirect or network coupling, rod/cone/rod, (Jin et al., 2020).
987 6. Cx36 in the ONL is very weak, indistinguishable from non-specific background labeling. If
988 any immunolabeling represents gap junctions, as opposed to non-specific noise, these very
989 low numbers are not enough to account for coupling between the multitude of rods

990

991 We conclude there is no direct rod/rod coupling in the mouse retina.

992

993

994 In summary, the evidence for the predominant role of rod/cone gap junctions is strong and
995 straightforward. In contrast, we found no evidence for rod/rod gap junctions and the distribution
996 of Cx36 does not match the location of rod/rod contacts. We were also unable to detect
997 cone/cone gap junctions by immunofluorescence or EM, but there is at least some supporting
998 physiological evidence in favor of cone/cone gap junctions. It may seem unsatisfactory that we
999 were unable to detect rod/rod or cone/cone gap junctions, but it does not change the main result:
1000 that rod/cone coupling accounts for the vast majority of photoreceptor gap junctions.

1001 **Appendix 2 –**

1002

1003 **Table 1**

	Whole cones		Inside cones		p-value
N of cones	29		13		
N of rods	811		361		
Rods / cone	28.0		27.8		
Convergence					
mean ± s.d.	43.0 ± 5.4		41.7 ± 4.2		0.40
median (Q1-Q3)	43 (39 - 46)		43 (38 - 45)		
Divergence	1.54 ± 0.63		1.89 ± 0.64		2.5×10^{-17}
Conv. / Div.	28.0		22.1		
Cone coverage area*					
mean ± s.d.	103 ± 20		102 ± 14		
median (Q1-Q3)	100 (86.7 - 117)		99.9 (93.0 - 111)		
Area covered by cones*	1920		890		
Cone density**	0.0151		0.0146		
Coverage	1.56		1.49		
N of shared rods					
mean ± s.d.	6.23 ± 4.67	(N=79)	5.85 ± 4.42	(N=61)	0.63
median (Q1-Q3)	4 (2 - 8)		5 (2 - 9)		

1004 Unit is *(μm^2) and **($/\mu m^2$).

1005

1006

1007 **Table 2**

	Blue cones		Green cones		p-value
N of cones	5		31		
Convergence					
mean ± s.d.	39.8 ± 5.11		43.0 ± 6.9		0.31
median (Q1-Q3)	39 (39 - 41)		43 (39 - 46)		
Cone coverage area*					
mean ± s.d.	85.1 ± 18.6		104 ± 22		0.081
median (Q1-Q3)	83.4 (76.4 - 98.0)		105 (84.8 - 120)		
N of shared rods					
mean ± s.d.	6.56 ± 6.34	(N=16)	6.26 ± 4.14	(N=69)	0.86
median (Q1-Q3)	6 (3 - 9)		3.5 (2 - 10.8)		

1008 *Unit is (μm^2).

1009

1010 **Table 3**

1011

FIB-SEM analysis	
N of rods	42
N of GJ / rod	
mean ± s.d.	3.21 ± 1.23
median (Q1-Q3)	3 (2 - 4)
GJ position*	
mean ± s.d.	0.686 ± 0.635
median (Q1-Q3)	0.435 (0.345 - 0.703)
Synaptic mouth radius*	0.138 ± 0.121
GJ width*	
mean ± s.d.	0.123 ± 0.032
median (Q1-Q3)	0.120 (0.103 - 0.138)
GJ length*	
mean ± s.d.	0.477 ± 0.227
median (Q1-Q3)	0.419 (0.332 - 0.568)
Total GJ length / rod*	
mean ± s.d.	1.53 ± 0.44
median (Q1-Q3)	1.52 (1.33 - 1.85)

1012 Unit is *(μm) and **(μm^2).

1013

1014 **Figure Legends**

1015

1016 **Figure 1 – The Distribution of Cx36 in the OPL**

1017

1018 **A.** Cx36 labeling in the OPL, confocal microscopy. Top left: numerous small Cx36 clusters
1019 (red) throughout the OPL, absent in the ONL. For all four panels: arrowheads, Cx36 under each
1020 cone pedicle, horizontal arrow, non-specifically labeled blood vessel. Top right: Cx36 clusters
1021 decorate the cone pedicles and their telodendria, labeled for cone arrestin (green). Lower left:
1022 Cx36 clusters are contained within the band of rod spherules, stained with an antibody against
1023 vGlut1 (blue). Lower right: 4 channels showing Cx36 (red), cone pedicles (green), and rod
1024 spherules (blue) all contained within the OPL. DAPI labeled nuclei (grey) show the well-
1025 organized ONL. Video 1 shows this data set.

1026

1027 **B.** Analysis of A shows Cx36 was contained in the OPL with virtually no labeling in the ONL.
1028 Cx36 (red) is restricted to the band of cone pedicles (green) and rod spherules (blue). A small
1029 Cx36 peak outside the cone curve corresponds to the Cx36 under the cones (arrowhead). The
1030 non-specifically labeled blood vessels were removed for this analysis. Cx36 clusters colocalized
1031 with cone pedicles (orange) fit within the cone arrestin curve.

1032

1033 **C.** EGFP labeled single cones (green) against a background of all cones stained for cone arrestin
1034 (red) and rod spherules (blue).

1035

1036 **D.** 3D reconstruction of a single cone pedicle with many telodendria. Right, colocalized Cx36
1037 clusters (red) on a single cone pedicle (green). Video 2 shows this data set.
1038
1039 **E.** A single confocal section showing that rod spherules (blue) occur close to the Cx36 clusters
1040 (red) located on a cone pedicle (green).
1041
1042 **F.** The number of Cx36 clusters, 51±8.9 (mean ± SD) on a single reconstructed cone pedicle,
1043 box shows quartiles, mean (circle), median (bold line), SD (whisker), min/max (x), n = 18.
1044
1045 **G.** Blue cone pedicle (cyan), identified in a blue cone opsin Venus mouse line, had telodendria
1046 bearing Cx36 clusters (red), similar to those of green cones, stained for cone arrestin (green).
1047
1048
1049 **Figure 2 – Cx36 clusters are found at the base of each Rod Spherule**
1050
1051 **A.** Top, detail of OPL, rod spherules, stained for vGlut1 (blue) and outlined with dashed lines
1052 are located above and between cone pedicles labeled for cone arrestin (green). Cx36 clusters
1053 (red) are found at the base of rod spherules where they contact cones. Multiple Cx36 clusters
1054 occur at some contacts, arrow. Bottom, Cx36 clusters are located on cone telodendria.
1055
1056 **B.** Top left, a rod spherule labeled for vGlut1 (blue), outlined with a dashed line, has two
1057 compartments (* and **). Top middle, bottom compartment is open at the base and contains two
1058 mGluR6 labeled rod bipolar dendrites, identifying the post-synaptic compartment. Top right, the

1059 upper compartment is filled with a large mitochondrion, labeled for TOMM20 (red). Lower left,
1060 the synaptic ribbon, labeled for ribeye (white), lies between the two compartments, arching over
1061 the post-synaptic compartment. Lower middle, the synaptic ribbon lies between the
1062 mitochondrion and the mGluR6 label. Bottom right, all four labels superimposed showing a
1063 typical rod spherule.
1064
1065 **C.** 18 rod spherules, aligned and superimposed. Taking the rod spherule as a clock face, Cx36
1066 clusters, (red with individual puncta marked +), are found at the base, 6 o'clock, along with cone
1067 telodendria (green). The two single +s at 3 o'clock and 9 o'clock are associated with other rod
1068 spherules and were excluded from the analysis.
1069
1070 **D.** Average rod spherule showing Cx36 and cone telodendria at the base with a fitted spline
1071 curve.
1072
1073 **E.** The distribution of label in each confocal channel along a linearized version of the spline
1074 curve. Where the vGlut1 label is low, indicating the opening to the post-synaptic compartment,
1075 the Cx36 (red) and cone (green) signals are high. The double peak for Cx36 indicates clusters on
1076 each side of the synaptic opening.
1077
1078 **F.** Scatterplot showing the number of Cx36 clusters, presumed to be gap junctions, per rod
1079 spherule from a sample of 135 rods, mean 2.4 $\pm$ 0.97, box shows quartiles, mean (circle), median
1080 (bold line), SD (whisker), min/max (x).
1081

1082 **G.** Data plotted as histogram showing the distribution of multiple Cx36 clusters per rod
1083 spherule, n=135.
1084
1085
1086 **Figure 3 – Map of Cone Pedicles shows Telodendria Overlap**
1087
1088 **A.** Map of 164 cone pedicles in e2006, boxes 1 and 2 (low density, also Fig. 4, suppl. 1) show
1089 reconstructed areas, dark outlines show reconstructed cone pedicles, 6 blue cone pedicles filled
1090 dark blue (Behrens et al., 2016).
1091
1092 **B.** Vertical section from e2006 showing rod spherules (3 shades of blue), above and in between
1093 cone pedicles (green).
1094
1095 **C.** Skeletons of all 29 reconstructed cone pedicles (thick outlines) showing overlapping
1096 telodendrial fields, individually colored. Thick outlines show solid part of cone pedicles.
1097
1098 **D.** Projection of C showing cone pedicles restricted to the OPL and axons ascending through the
1099 ONL.
1100
1101
1102 **Figure 4 – Cone Skeleton Analysis shows Cones contact all nearby Rod Spherules**
1103

1104 **A.** Skeletons of one green cone (cone 5, green) and one blue cone (cone 2, blue) in wholemount
1105 view and projected. Arrows show ascending axon. The position of each contacted rod spherule
1106 is marked by a dot, color coded the same color (green or blue) if the contacts are exclusive to this
1107 cone pedicle, black, contacts 2 cones, grey, contacts 3 cones.
1108
1109 **B.** Telodendrial fields of 29 reconstructed cone pedicles, each color-coded, central 13 outlined
1110 by polygons, arrow points to blue cone (cone 2).
1111
1112 **C.** Outlines of central 13 cone pedicles showing all rod spherule contacts, color coded, exclusive
1113 to one cone, black, contacts with 2 cones, dark grey, contacts with three cones. Light grey, rod
1114 spherules outside the range of the central 13 cone pedicles.
1115
1116 **D.** Simplified skeleton map showing contacts of two cone green pedicles (cones 3 and 5), the
1117 box contains the cone identity, the total number of rod contacts (above) and the exclusive
1118 number of rods which contact this cone only. Circles indicate the number of rod spherules
1119 shared between cones linked by lines to neighbors. Cone 2 is a blue cone, which shares rod
1120 contacts with neighboring cones.
1121
1122 **E.** Pie chart showing distribution of cone contacts per rod spherule.
1123
1124 **F.** Convergence, rod contacts per cone for all 29 reconstructed cone pedicles, inner 13 and 5
1125 blue cones. Box shows quartiles, mean (circle), median (bold line), SD (whisker), min/max (x).
1126

1127 **G.** Cone pedicle telodendrial field area for all 29 reconstructed cone pedicles, inner 13 and 5
1128 blue cones. Box shows quartiles, mean (circle), median (bold line), SD (whisker), min/max (x).
1129
1130 **H.** Convergence vs cone pedicle area. Line of linear regression shows some tendency for larger
1131 cone pedicles to contact more rods. +, blue cones
1132
1133
1134 **Figure 5 – Segmentation and 3D Reconstruction e2006: Cone Telodendria contact Rod**
1135 **Spherules close to the Mouth of the Synaptic Opening**
1136
1137 **A.** Single SBF-SEM section, telodendria from 2 cones (green or cyan), rod spherule (pink), in
1138 the plane of the synaptic opening with cone contacts on both sides.
1139
1140 **B.** Single SBF-SEM section, rod spherule (blue), post-synaptic inclusions show it is close to the
1141 synaptic opening, 25 nm x 4 sections = 100 nm away. The rod spherule sits on the roof of a cone
1142 pedicle (green) with a contact, shown by the arrow, where membranes merge.
1143
1144 **C.** Single SBF-SEM section, rod spherule (magenta) with contacts at the synaptic opening from
1145 2 different cones (green or cyan).
1146
1147 **D.** Single SBF-SEM section, rod spherule (orange), contacts (arrow) the roof of a cone pedicle
1148 (green) with a telodendrial contact (arrowhead) from a second cone (cyan). Post-synaptic

1149 inclusions in the rod spherule indicate the contacts are close to the synaptic opening, 25 nm x 9
1150 sections = 225 nm away.
1151
1152 **E.** Top, confocal microscopy, single optical section, shows Cx36 clusters (red) where
1153 telodendria from 2 different cones (white for cone arrestin, labels both cones; green for a single
1154 EGFP labeled cone) contact rod spherule (blue), at the mouth of the synaptic opening. Bottom,
1155 cone arrestin signal turned off for clarity, showing only one cone is labeled for EGFP.
1156
1157 **F.** 3D reconstruction from e2006, 2 adjacent green cone pedicles (cone 5, green, and cone 3,
1158 cyan), ghost cell bodies (grey) show limits of ONL and INL, arrow marks ascending cone axons.
1159
1160 **G.** Same 2 cone pedicles with all 66 (= 38 + 34 – 6 shared) reconstructed rod spherules
1161 contacted by these 2 cones.
1162
1163 **H.** Rotated view, looking down at top surface of same 2 cone pedicles, contact pads with rod
1164 spherules marked in red or yellow for each cone.
1165
1166 **I.** Rotated view, looking up at the bottom surface of all rod spherules in contact with these 2
1167 cones, contact pads in red or yellow, arrow head marks a single rod spherule magnified in J and
1168 K.
1169
1170 **J.** Single rod spherule (pink), green cone pedicle (cone 5), with adjusted transparency, with
1171 contact pad (red) encircling the synaptic opening at the base of the rod spherule (arrowhead).

1172 The second cone (cone 3, cyan) also contacts this rod spherule nearby (yellow), approximately
1173 1μm from the synaptic mouth.
1174
1175 **K.** Detail, showing the bottom surface of 3 adjacent rod spherules which receive contacts close
1176 to the synaptic opening from both cone pedicles, contact pads in red or yellow, arrows show rod
1177 axons, arrowhead indicates same rod spherule as J.
1178 Video 5 shows this data set.
1179
1180
1181 **Figure 6 – Segmentation and 3D reconstruction shows Gap Junctions at Rod/Cone**
1182 **Contacts**
1183
1184 **A.** Singer dataset, SBF-SEM, a rod spherule (blue) nestled on the roof of a cone pedicle (green)
1185 with a densely stained gap junction contact (arrow).
1186
1187 **B.** Singer dataset, SBF-SEM, detail showing a gap junction (arrow) with merged membranes.
1188 Note, there is clear separation except at this point. Post-synaptic inclusions indicate the gap
1189 junction is close to the synaptic opening of the rod spherule.
1190
1191 **C.** FIB-SEM: Dense gap junction staining at contact points (arrows) between cone telodendria
1192 (green) and a rod spherule (blue). Inset: rotated en face view of one gap junction to measure
1193 length.
1194

1195 **D.** FIB-SEM: second example (arrow) of a dense gap junction at a cone contact (green) with a
1196 rod spherule (blue). Inset: en face view of the gap junction. Note green cone telodendrial
1197 contact exceeds the gap junction staining.
1198
1199 **E.** FIB-SEM: Overview of a rod spherule (blue) with a transparent reconstruction over the
1200 image planes in F and G. Note the large mitochondrion towards the top of the rod spherule.
1201
1202 **F.** Image plane of the rod spherule (blue) through the synaptic opening with a small gap junction
1203 on each side (arrows) at a cone contact (green).
1204
1205 **G.** Image plane close to the base of the rod spherule (blue) reveals the 2 small gap junctions in F
1206 are part of a single large gap junction. There is a horseshoe-shaped gap junction (arrow) close to
1207 the synaptic opening where a cone telodendron (green) wraps around the base of the rod
1208 spherule. Large Cx36 horse-shoe shaped Cx36 clusters like this are easily observed by confocal
1209 microscopy.
1210
1211 **H.** FIB-SEM 3D reconstruction of the rod spherule (transparent blue) showing a single large gap
1212 junction (red, arrow) around the synaptic opening at the base. Post-synaptic inclusions are also
1213 rendered with 2 rod bipolar dendrites (grey and cyan) and 2 horizontal cell processes (green and
1214 purple). The synaptic ribbon is shown in yellow, partially obscured by the post-synaptic
1215 processes.
1216 Video 6 shows this data set.
1217

1218

1219

1220 **Figure 7 – Quantitative Analysis of 42 Reconstructed Rod Spherules from FIB-SEM**

1221

1222 **A.** The number of gap junctions per rod spherule ranged from 1-6 (3.2 ± 1.2, mean ± SD, n=42).

1223 Box shows quartiles, mean (circle), median (bold line), SD (whisker), min/max (x).

1224

1225 **B.** Gap junction distance from the rod spherule synaptic opening, skewed distribution, median,

1226 0.44 μm. Box shows quartiles, mean (circle), median (bold line), SD (whisker), min/max (x).

1227

1228 **C.** Histogram plots of gap junction position, grey area shows diameter of the synaptic opening,

1229 (0.28±0.024μm, n=42 rod spherules)

1230

1231 **D.** Gap junction length vs width for 135 gap junctions from 42 rod spherules. Note restricted

1232 width compared to much greater variability in length, consistent with string-like structure. Box

1233 shows quartiles, mean (circle), median (bold line), SD (whisker), min/max (x) for width and

1234 length. Outliers in red are from rod spherules with a single large gap junction.

1235

1236 **E.** Total gap junction length per rod for 42 rod spherules. Box shows quartiles, mean (circle),

1237 median (bold line), SD (whisker), min/max (x).

1238

1239 **F.** Average gap junction length plotted as a function of the number of gap junctions per rod

1240 shows that if there is only one gap junction per rod spherule, it is a large one. The 2 longest gap

1241 junctions from D were both singles (red, same two as in D). These are easily observed when
1242 labeled for Cx36 using confocal microscopy (Fig. 1, suppl 2; Jin et al., 2020). The dashed line is
1243 the median gap junction length (0.42μm) and it runs through the data for multiple gap junctions
1244 per rod. In other words, each additional gap junction is approximately a standard size.
1245
1246 **G.** Total gap junction length per rod spherule as a function of the number of gap junctions per
1247 rod shows that the single gap junctions (red) are outliers with a large area. Total gap junction
1248 area tends to rise with the number of gap junctions. The straight line of linear regression shows
1249 the effect of adding a standard mean gap junction length (0.44μm) each time and runs through all
1250 the data except for the singles (red). Fitted line is $y = 0.44x$; ($R^2 = 0.33$).
1251
1252
1253 **Figure 8 - Cartoon Summary of Rod/Cone Gap Junctions in the Mouse Retina**
1254
1255 A cartoon showing the variety of Cx36 rod/cone gap junctions, including cone telodendrial
1256 contacts, cone pedicle roof contacts and inverted rod spherules. The lowest row of rod cell
1257 bodies in the ONL do not have rod spherules but still have Cx36 gap junctions with cone
1258 telodendria, which reach the upper margin of the OPL. All these structural variants were also
1259 found with blue cone pedicles indicating there was no color specificity in rod/cone coupling.
1260 Most rod spherules have gap junction contacts with more than one cone. All rod spherules, with
1261 very few exceptions (such as areas of low cone density), make gap junctions with nearby cone
1262 pedicles. In contrast to the numerous rod/cone gap junctions, we could not detect rod/rod or
1263 cone/cone gap junctions in these experiments.

1264 ## Supplementary Figure Legends

1265

1266

1267 **Figure 1, supplement 1 – The distribution of blue cone opsin in the mouse retina**

1268

1269 Wholemount view of whole blue cone opsin Venus mouse retina shows most cones in ventral

1270 retina express blue cone opsin. In the dorsal retina, there is a sparse mosaic of true blue cones.

1271

1272

1273 **Figure 1, supplement 2 – Blue cone pedicles have telodendria bearing Cx36 clusters.**

1274

1275 **A.** Dorsal retina of a blue cone opsin Venus mouse contains a sparse set of true-blue cones

1276 (cyan) among the majority of green cones labeled for cone arrestin (green).

1277

1278 **B.** Zoom in on one blue cone pedicle shows Cx36-labeled (red) telodendria. Surrounding green

1279 cone pedicles labeled for cone arrestin (green). Large red structures are non-specifically labeled

1280 blood vessels.

1281

1282 **C.** Outer segments showing a sparse set of cones labeled with an antibody against blue cone

1283 opsin (cyan). Background of green cones labeled for cone arrestin (green).

1284

1285 **D.** Following the cone axons through a series of confocal images allows the blue cone pedicles

1286 to be identified (asterisks), see supplementary movie 3 from Fig. 1, supplement 2.

1287

1288 **E.** Enlarged view of a single blue cone pedicle (asterisk) with Cx36 (red) labeled telodendria,

1289 comparable to the surrounding green cones labeled for cone arrestin (green)

1290

1291

1292 **Figure 4, supplement 1 – Nearly All Rods receive Cone Contacts**

1293

1294 **A.** Map showing telodendria of all 29 cone pedicles (Fig. 3A, box 1), each individually colored,

1295 dots mark all rod spherules in contact, same color as cone if contacts are exclusive to one cone,

1296 black, contact with two cones, grey, contact with 3 cones, light grey no contacts, mostly outside

1297 the field of all 29 cones. Within the field of 29 cones, there were 811 rod spherules of which 808

1298 (99.6%) received cone contacts. 3/811 (0.4%) rod spherules received no cone contacts.

1299

1300 **B.** Removing cone pedicles and rod spherules in contact with the central 13 cone pedicles,

1301 leaves a hole with no remaining rod spherules (0/361) inside an annulus of rod spherules outside

1302 the field of the central 13 cones. The telodendrial field of cone 5 (green, axon removed) is shown

1303 for comparison.

1304

1305 **C.** Polygons outline the telodendrial fields of 6 cones in a sparse region (Fig.3A, box 2). In the

1306 center, there is a rare hole in the cone coverage, almost like a cone is missing.

1307

1308 **D.** Removing cones and plotting rod spherules, (color coded by cone for exclusive contacts,

1309 black, two cones, dark grey, three cones, no contacts, light grey) reveals 8/175 (4.6%) of rod

1310 spherules in the central area with no cone contacts. This may represent a local upper limit of rods
1311 without cone contacts, since we deliberately chose a sparse area.
1312
1313
1314 **Figure 4, supplement 2 – Rod Connectivity Map for 29 Cone Pedicles**
1315
1316 **A.** Full connectivity map for all 29 cone pedicles that were reconstructed, central 13 clear boxes,
1317 outer 16, shaded boxes. Each square represents one cone, containing the identity with the total
1318 number of rod contacts above, 43 ± 5.4 (mean ± SD, n=29) and the number of exclusive contacts
1319 below, 7.2 ± 3.4 (mean ± SD, n=13, central cones only; outer cone numbers for exclusive
1320 contacts are high due to edge effects). Circles show number of rod spherules shared between
1321 cone pedicles connected by lines. Most cone pedicles share rod spherules with all neighboring
1322 cones. Cones 5 (green), 3 (cyan) & 2 (blue) were segmented and reconstructed in 3D. Cone 2 is
1323 a blue cone (Behrens et al., 2016).
1324
1325 **B.** The number of rod spherules shared between any two adjacent cone pairs, 6.2 ± 4.7 (mean ±
1326 SD, n=79 pairs among all 29 cones, black), central 13 cones (red) (5.9 ± 4.4, mean ± SD, n=61
1327 pairs); blue cones, 6.6 ± 6.3 (mean ± SD, n=16 pairs from 5 blue cones). Box shows quartiles,
1328 mean (circle), median (bold line), SD (whisker), min/max (x).
1329
1330 *79 pairs from the 29 cones include GC-GC and BC-GC pairs while blue cone data shows BC-
1331 GC pairs only. Note that there are no BC-BC pairs. GC, green cone, BC, blue cone. Table 2,

1332 Appendix 2, additionally shows statistics for only GC-GC pairs, 6.3 ± 4.1 (mean ± SD, n=69
1333 pairs from 31 green cones), (27 GC of the 29 cones and 4 GC in sparse density area).
1334
1335
1336 **Figure 5, supplement 1 – Confocal Microscopy, Roof Contacts**
1337
1338 **A.** Cx36 clusters (red) occur where 3 rod spherules (vGlut1, blue) make contact (arrows) with
1339 the upper surface or roof of a single EGFP labelled cone (green). Each of these probable gap
1340 junctions is close to the opening of a rod spherule post-synaptic compartment.
1341
1342
1343 **Figure 5, supplement 2 – Low Rods**
1344
1345 **A.** Confocal microscopy, 3 rod somas, labelled with DAPI, (grey, asterisks) in the lowest row of
1346 the ONL adjacent to the upper margin of the OPL, have no axons or spherules. Instead, the
1347 synaptic machinery, stained with vGlut1 (blue), is contained in a crescent at the base (Li et al.,
1348 2016). Cone telodendria, stained for cone arrestin (green) contact each of these rods with Cx36
1349 clusters (arrows, red) at the contact points, close to the mouth of the synaptic opening.
1350
1351 **B.** Segmentation from e2006, single sections; left, a rod soma from the lowest row of the ONL
1352 contains post-synaptic inclusions at the base and receives contact from a cone telodendron
1353 (green) close to the post-synaptic opening (25nm x 7 sections = 175 nm away); right, a similar
1354 example, a low rod soma, (brown) with a post-synaptic compartment at the base receives

1355 contacts from two different cones (green and cyan) (16.5 nm x 5 sections = 82.5 nm to the post-
1356 synaptic opening).
1357
1358 **C.** 3D reconstruction of the 5 rods in the lowest row of the ONL above cones 5 & 3, (a subset of
1359 the rods in Fig. 5G) shows they sit on a nest of up-reaching cone telodendria. For comparison, a
1360 rod spherule (blue) is included, far left, arrowhead. Arrows, axon ascending from rod spherule
1361 and cone 5 axon (green).
1362
1363 **D.** The same 5 low rods rotated to view the cone telodendrial contact pads (yellow or red)
1364 around the mouth of the post-synaptic compartment on the lower surface of each rod. Arrows
1365 show axons. Inset for size comparison, a reconstructed rod spherule.
1366
1367
1368 **Figure 5, supplement 3 – Low Rod Spherules**
1369
1370 **A.** Confocal microscopy, OPL, a cone pedicle and telodendria stained for cone arrestin (green)
1371 and a cluster of rod spherules, stained for vGlut1(blue) and outlined for Plasma Membrane
1372 Calcium ATPase (PMCA) (yellow). Cx36 clusters (red) occur at cone contacts with the base of
1373 each rod spherule, close to the synaptic opening (arrowheads). One rod spherule is very low and
1374 protrudes below the level of the cone pedicle. This rod spherule is rotated horizontally so the
1375 post-synaptic opening is adjacent to the cone pedicle and there is a Cx36 cluster at this contact
1376 site (arrow). Thus, the rule is that rod/cone contacts occur close to the rod spherule post-synaptic
1377 opening, whatever the orientation.

1378

1379 **B.** Segmentation, e2006 dataset, a low rod spherule (pink) is inverted to receive a cone contact

1380 (green) close to the synaptic opening (arrowhead), 25 nm x 24 frames = 600 nm away.

1381

1382 **C.** An inverted rod spherule (orange), adjacent to a cone pedicle (green) but with clear

1383 membrane separation and no contact, receives cone telodendrial contacts (cyan) near the synaptic

1384 opening, (25 nm x 12 frames = 300 nm away) which in this case is uppermost.

1385

1386 **D.** 3D reconstruction e2006, a low rod spherule (purple) is inverted and receives a cone contact

1387 (green, transparent), close to the post-synaptic mouth. Arrows indicate cone axon and rod axon,

1388 ascending to rod soma.

1389

1390 **E.** Detail showing the contact pad (red) curved around the post-synaptic opening.

1391

1392

1393 **Figure 5, supplement 4 – Blue Cones, Segmentation, e2006**

1394

1395 **A.** Detail of cone pedicle skeletons from Fig. 4 with the field of cone 2 outlined. This cone was

1396 identified as a blue cone by Behrens et al (2016). Arrow shows axon.

1397

1398 **B.** Segmentation, e2006, blue cone pedicle (cone 2, dark blue) makes a variety of contacts with

1399 nearby rod spherules. 1. Telodendrial contacts close to the synaptic mouth of 4 rod spherules.

1400 2. A roof contact, arrow, with a rod spherule (green). 3. Telodendrial contacs with a low rod

1401 (cyan) in the lowest row of the ONL. The contacts of blue cone pedicles are indistinguishable
1402 from green cones.
1403
1404
1405 **Figure 5, supplement 5 – Blue Cones e2006, 3D Reconstruction**
1406
1407 **A.** Reconstructed cone pedicles (cone 5, green and cone 2, dark blue, arrowhead, identified as a
1408 blue cone by Behrens et al (2016)). Arrows indicate ascending axons among ghost cells of the
1409 ONL (grey).
1410
1411 **B.** The block of rods receiving contacts from 3 adjacent cone pedicles, cones 5 (green), cone 3
1412 (cyan) and blue cone 2 (dark blue).
1413
1414 **C.** Rotated view showing the top surface of these 3 cone pedicles with contact pads in red,
1415 yellow and orange. Arrows indicate ascending axons, arrowhead shows a ring-like structure of
1416 contacts.
1417
1418 **D.** Rotated view, bottom surface of the rod spherules with contact pads, arrow head marks same
1419 ring of contacts, as in C.
1420
1421 **E**. Detail, several rod spherules receiving contacts from the blue cone 2, orange, and cone 3,
1422 yellow. Rod spherules receive contacts indiscriminately from blue and green cones or both
1423 simultaneously. Arrows mark cone axons.

1424

1425

1426 **Figure 7, supplement 1 – Rod/rod and cone/cone contacts do not appear as gap junctions,**

1427 **FIB-SEM**

1428

1429 **A.** Partial reconstruction of 6 cone pedicles from FIB-SEM.

1430 **B.** Examples of cone/cone contacts (coral/blue or yellow/cyan, arrows), which show no

1431 membrane density. These examples were selected because of the nearby rod/cone contacts

1432 (arrowheads) which show prominent dense staining at their contact points, consistent with the

1433 presence of a gap junction.

1434

1435 **C.** Rod/rod contacts (coral/magenta, arrows) show no membrane specialization, compared to

1436 nearby rod/cone gap junctions (coral/green, arrowheads).

Videos

Video 1 from Fig. 1A

Animation of a confocal series from the OPL showing Cx36 (red) decorating the cone telodendria (green, cone arrestin). All Cx36 clusters fall within the band of vGlut1 (blue) labeled rod spherules. No Cx36 in the ONL.

Video 2 from Fig. 1D

3D reconstruction of a single EGFP labeled cone pedicle among all cone arrestin (blue) labeled cones, with extensive telodendria. All the Cx36 clusters in the OPL, then only those Cx36 clusters, more than 50, colocalized with the single EGFP labeled cone pedicle. Cx36 is distributed along the telodendria, often at the tips, and on the upper surface or roof of the cone pedicle.

Video 3 from Fig. 1, supplement 2

Animating from the OPL to the outer segments following the cone axon allows cone labeled for blue cone opsin to be connected to its pedicle, labeled for cone arrestin.

Video 4

3D reconstruction of a single cone (cone 5, green) with contact pads in red, then all rod spherules which were in contact with this cone.

Video 5 from Fig. 5F – K

A pair of reconstructed adjacent cone pedicles (cone 5, green, & cone 3, cyan). A rotated view shows the contact pads from the top of the cone, then the contact pads from the bottom of the rod spherules, zooming in to show how a contact pad is close to the post-synaptic opening.

Video 6 from Fig. 6H

3D reconstruction showing a large horseshoe-shaped gap junction (red) around the base of a transparent rod spherule with post-synaptic processes also filled (from FIB-SEM)

Source data

Figure 1 – source data 1

Number of Cx36 clusters on a single cone pedicle.

Source data for Figure 1F.

Figure 2 – source data 1

Number of Cx36 clusters on a rod spherule.

Source data for Figure 2F, G.

Figure 3 – source data 1

Cone pedicle skeletons and rod spherule points.

Knossos data file of skeletons for Figure 3, 4.

Figure 4 – source data 1

Cone coverage area and rod convergence.

Source data for Figure 4F-H.

Figure 4 – source data 2

The number of rod spherules shared between two adjacent cone pairs.

Source data for Figure 4 – supplement 2B.

1502 **Figure 7 – source data 1**

1503 **Quantitative analysis of rod spherules from FIB-SEM**

1504 Source data for Figure 7A-G.

1505

1506

1507 Data availability

1508

1509 All the data used to create the figures in the manuscript have been provided as source data files

1510 for Figures 1, 2, 3, 4, and 7.

1511

1512 The following data sets were generated. **In Process.**

1513

1514 Ishibashi M, Keung J, Ribelayga CP, Massey SC (2018) Confocal imaging of the outer

1515 plexiform layer in mouse retina. ID:xxx. URL:xxxx In the public domain at BIL

1516 http://www.brainimagelibrary.org/index.html

1517

1518 Singer JH (2018) SBF-SEM of mouse retina. eel001. URL:xxxx In the public domain at

1519 webKnossos https://webknossos.org/

1520

1521 Morgan CW, Aicher SA, Carroll JR (2019) FIB-SEM of the outer plexiform layer in light-

1522 adapted mouse retina. EM1 and EM2, ID:xxx. URL:xxxx In the public domain at BossDB

1523 https://bossdb.org/

References

Asteriti S, Gargini C, Cangiano L. 2017. Connexin 36 expression is required for electrical coupling between mouse rods and cones. *Vis Neurosci* **34**:E006. doi:10.1017/S0952523817000037

Asteriti S, Gargini C, Cangiano L. 2014. Mouse rods signal through gap junctions with cones. *Elife* **3**. doi:10.7554/eLife.01386

Behrens C, Schubert T, Haverkamp S, Euler T, Berens P. 2016. Connectivity map of bipolar cells and photoreceptors in the mouse retina. *Elife* **5**. doi:10.7554/ELIFE.20041

Belevich I, Joensuu M, Kumar D, Vihinen H, Jokitalo E. 2016. Microscopy Image Browser: A Platform for Segmentation and Analysis of Multidimensional Datasets. *PLOS Biol* **14**:e1002340. doi:10.1371/journal.pbio.1002340

Beyer EC, Berthoud VM. 2009. The Family of Connexin Genes.In: Connexins: A Guide, A. Harris, D. Locke (Eds.), Humana Press, New York (2009),. pp. 3–26.

Bloomfield SA, Völgyi B. 2009. The diverse functional roles and regulation of neuronal gap junctions in the retina. *Nat Rev Neurosci* **10**:495–506. doi:10.1038/nrn2636

Bolte P, Herrling R, Dorgau B, Schultz K, Feigenspan A, Weiler R, Dedek K, Janssen-Bienhold U. 2016. Expression and Localization of Connexins in the Outer Retina of the Mouse. *J Mol Neurosci* **58**:178–192. doi:10.1007/s12031-015-0654-y

Carter-Dawson LD, Lavail MM. 1979. Rods and cones in the mouse retina. I. Structural analysis using light and electron microscopy. *J Comp Neurol* **188**:245–262. doi:10.1002/cne.901880204

Connors BW. 2017. Synchrony and so much more: Diverse roles for electrical synapses in neural

circuits. *Dev Neurobiol* **77**:610–624. doi:10.1002/dneu.22493

Dacey DM, Lee BB. 1994. The "blue-on" opponent pathway in primate retina originates from a distinct bistratified ganglion cell type. *Nature* **367**:731–735. doi:10.1038/367731a0

Dang L, Pulukuri S, Mears AJ, Swaroop A, Reese BE, Sitaramayya A. 2004. Connexin 36 in photoreceptor cells: Studies on transgenic rod-less and cone-less mouse retinas. *Mol Vis* **10**:323–327.

DeVries SH, Qi X, Smith R, Makous W, Sterling P. 2002. Electrical coupling between mammalian cones. *Curr Biol* **12**:1900–1907. doi:10.1016/S0960-9822(02)01261-7

Ecker JL, Dumitrescu ON, Wong KY, Alam NM, Chen SK, LeGates T, Renna JM, Prusky GT, Berson DM, Hattar S. 2010. Melanopsin-expressing retinal ganglion-cell photoreceptors: Cellular diversity and role in pattern vision. *Neuron* **67**:49–60. doi:10.1016/J.NEURON.2010.05.023

Feigenspan A, Janssen-Bienhold U, Hormuzdi S, Monyer H, Degen J, Söhl G, Willecke K, Ammermüller J, Weiler R. 2004. Expression of Connexin36 in Cone Pedicles and OFF-Cone Bipolar Cells of the Mouse Retina. *J Neurosci* **24**:3325–3334. doi:10.1523/JNEUROSCI.5598-03.2004

Field GD, Greschner M, Gauthier JL, Rangel C, Shlens J, Sher A, Marshak DW, Litke AM, Chichilnisky EJ. 2009. High-sensitivity rod photoreceptor input to the blue-yellow color opponent pathway in macaque retina. *Nat Neurosci* **12**:1159–64. doi:10.1038/nn.2353

Field GD, Uzzell V, Chichilnisky EJ, Rieke F. 2019. Temporal resolution of single-photon responses in primate rod photoreceptors and limits imposed by cellular noise. *J Neurophysiol* **121**:255–268. doi:10.1152/jn.00683.2018

Haverkamp S, Wässle H, Duebel J, Kuner T, Augustine GJ, Feng G, Euler T. 2005. The

primordial, blue-cone color system of the mouse retina. *J Neurosci* **25**:5438–5445. doi:10.1523/JNEUROSCI.1117-05.2005

Helmstaedter M, Briggman KL, Denk W. 2011. High-accuracy neurite reconstruction for high-throughput neuroanatomy. *Nat Neurosci* **14**:1081–1088. doi:10.1038/nn.2868

Helmstaedter M, Briggman KL, Turaga SC, Jain V, Seung HS, Denk W. 2013. Connectomic reconstruction of the inner plexiform layer in the mouse retina. *Nature* **500**:168–174. doi:10.1038/nature12346

Hornstein EP, Verweij J, Schnapf JL. 2004. Electrical coupling between red and green cones in primate retina. *Nat Neurosci* **7**:745–750. doi:10.1038/nn1274

Hsu A, Smith RG, Buchsbaum G, Sterling P. 2000. Cost of cone coupling to trichromacy in primate fovea. *J Opt Soc Am A Opt Image Sci Vis* **17**:635–40. doi:10.1364/josaa.17.000635

Ingram NT, Sampath AP, Fain GL. 2019. Voltage-clamp recordings of light responses from wild-type and mutant mouse cone photoreceptors. *J Gen Physiol* **151**:1287–1299. doi:10.1085/jgp.201912419

Jin N, Zhang Z, Keung J, Youn SB, Ishibashi M, Tian L-M, Marshak DW, Solessio E, Umino Y, Fahrenfort I, Kiyama T, Mao C-A, You Y, Wei H, Wu J, Postma F, Paul DL, Massey SC, Ribelayga CP. 2020. Molecular and functional architecture of the mouse photoreceptor network. *Sci Adv* **6**:eaba7232. doi:10.1126/sciadv.aba7232

Jin NG, Chuang AZ, Masson PJ, Ribelayga CP. 2015. Rod electrical coupling is controlled by a circadian clock and dopamine in mouse retina. *J Physiol* **593**:1597–1631. doi:10.1113/jphysiol.2014.284919

Jin NG, Ribelayga CP. 2016. Direct Evidence for Daily Plasticity of Electrical Coupling between Rod Photoreceptors in the Mammalian Retina. *J Neurosci* **36**:178–84.

doi:10.1523/JNEUROSCI.3301-15.2016

Johnson JE, Perkins GA, Giddabasappa A, Chaney S, Xiao W, White AD, Brown JM, Waggoner J, Ellisman MH, Fox DA. 2007. Spatiotemporal regulation of ATP and Ca2+ dynamics in vertebrate rod and cone ribbon synapses. *Mol Vis* **13**:887–919.

Kamasawa N, Furman CS, Davidson KGV, Sampson JA, Magnie AR, Gebhardt BR, Kamasawa M, Yasumura T, Zumbrunnen JR, Pickard GE, Nagy JI, Rash JE. 2006. Abundance and ultrastructural diversity of neuronal gap junctions in the OFF and ON sublaminae of the inner plexiform layer of rat and mouse retina. *Neuroscience* **142**:1093–1117. doi:10.1016/j.neuroscience.2006.08.020

Kántor O, Benkő Z, Énzsöly A, Dávid C, Naumann A, Nitschke R, Szabó A, Pálfi E, Orbán J, Nyitrai M, Németh J, Szél Á, Lukáts Á, Völgyi B. 2016. Characterization of connexin36 gap junctions in the human outer retina. *Brain Struct Funct* **221**:2963–2984. doi:10.1007/S00429-015-1082-Z

Kolb H. 1977. The organization of the outer plexiform layer in the retina of the cat: electron microscopic observations. *J Neurocytol* **6**:131–153. doi:10.1007/BF01261502

Kothmann WW, Massey SC, O'Brien J. 2009. Dopamine-stimulated dephosphorylation of connexin 36 mediates AII amacrine cell uncoupling. *J Neurosci* **29**:14903–11. doi:10.1523/JNEUROSCI.3436-09.2009

Kouyama N, Marshak DW. 1992. Bipolar cells specific for blue cones in the macaque retina. *J Neurosci* **12**:1233–52. doi:10.1523/JNEUROSCI.12-04-01233.1992

Koval M, Molina SA, Burt JM. 2014. Mix and match: Investigating heteromeric and heterotypic gap junction channels in model systems and native tissues. *FEBS Lett* **588**:1193–1204. doi:10.1016/J.FEBSLET.2014.02.025

Lasseigne AM, Echeverry FA, Ijaz S, Michel JC, Martin EA, Marsh AJ, Trujillo E, Marsden KC, Pereda AE, Miller AC. 2021. Electrical synaptic transmission requires a postsynaptic scaffolding protein. *Elife* **10**. doi:10.7554/ELIFE.66898

Li H, Zhang Z, Blackburn MR, Wang SW, Ribelayga CP, O'Brien J. 2013. Adenosine and dopamine receptors coregulate photoreceptor coupling via gap junction phosphorylation in mouse retina. *J Neurosci* **33**:3135–3150. doi:10.1523/JNEUROSCI.2807-12.2013

Li PH, Verweij J, Long JH, Schnapf JL. 2012. Behavioral/Systems/Cognitive Gap-Junctional Coupling of Mammalian Rod Photoreceptors and Its Effect on Visual Detection. doi:10.1523/JNEUROSCI.2144-11.2012

Li S, Mitchell J, Briggs DJ, Young JK, Long SS, Fuerst PG. 2016. Morphological diversity of the rod spherule: A study of serially reconstructed electron micrographs. *PLoS One* **11**:e0150024. doi:10.1371/journal.pone.0150024

Li W. 2020. Ground squirrel – A cool model for a bright vision. *Semin Cell Dev Biol* **106**:127–134. doi:10.1016/j.semcdb.2020.06.005

Li W, Chen S, Devries SH. 2010. A fast rod photoreceptor signaling pathway in the mammalian retina. *Nat Neurosci* **13**:414–416. doi:10.1038/nn.2507

Li W, DeVries SH. 2004. Separate blue and green cone networks in the mammalian retina. *Nat Neurosci* **7**:751–756. doi:10.1038/nn1275

Marandykina A, Palacios-Prado N, Rimkutė L, Skeberdis VA, Bukauskas FF. 2013. Regulation of connexin36 gap junction channels by n -alkanols and arachidonic acid. *J Physiol* **591**:2087–2101. doi:10.1113/jphysiol.2013.250910

Marc RE, Liu WLS, Muller JF. 1988. Gap junctions in the inner plexiform layer of the goldfish retina. *Vision Res* **28**:9–24.

Marc RE, Sigulinsky CL, Pfeiffer RL, Emrich D, Anderson JR, Jones BW. 2018. Heterocellular coupling between amacrine cells and ganglion cells. *Front Neural Circuits* **12**. doi:10.3389/FNCIR.2018.00090

Miller AC, Pereda AE. 2017. The electrical synapse: Molecular complexities at the gap and beyond. *Dev Neurobiol* **77**:562–574. doi:10.1002/DNEU.22484

Miller AC, Whitebirch AC, Shah AN, Marsden KC, Granato M, O'Brien J, Moens CB. 2017. A genetic basis for molecular asymmetry at vertebrate electrical synapses. *Elife* **6**. doi:10.7554/eLife.25364

Nadal-Nicolás FM, Kunze VP, Ball JM, Peng BT, Krisnan A, Zhou G, Dong L, Li W. 2020. True S-cones are concentrated in the ventral mouse retina and wired for color detection in the upper visual field. *Elife* **9**:1–30. doi:10.7554/eLife.56840

Nagy JI, Pereda AE, Rash JE. 2018. Electrical synapses in mammalian CNS: Past eras, present focus and future directions. *Biochim Biophys acta Biomembr* **1860**:102–123. doi:10.1016/j.bbamem.2017.05.019

Nelson R. 1977. Cat cones have rod input: A comparison of the response properties of cones and horizontal cell bodies in the retina of the cat. *J Comp Neurol* **172**:109–135. doi:10.1002/cne.901720106

O'Brien J. 2014. The ever-changing electrical synapse. *Curr Opin Neurobiol* **29**:64–72. doi:10.1016/j.conb.2014.05.011

O'Brien JJ, Chen X, Macleish PR, O'Brien J, Massey SC. 2012. Photoreceptor coupling mediated by connexin36 in the primate retina. *J Neurosci* **32**:4675–4687. doi:10.1523/JNEUROSCI.4749-11.2012

Pallotto M, Watkins P V., Fubara B, Singer JH, Briggman KL. 2015. Extracellular space

preservation aids the connectomic analysis of neural circuits. *Elife* **4**. doi:10.7554/eLife.08206

Paridaen JTML, Wilsch-Bräuninger M, Huttner WB. 2013. XAsymmetric inheritance of centrosome-associated primary cilium membrane directs ciliogenesis after cell division. *Cell* **155**:333. doi:10.1016/j.cell.2013.08.060

Quraishi S, Gayet J, Morgans CW, Duvoisin RM. 2007. Distribution of group-III metabotropic glutamate receptors in the retina. *J Comp Neurol* **501**:931–43. doi:10.1002/cne.21274

Raviola E, Gilula NB. 1973. Gap junctions between photoreceptor cells in the vertebrate retina. *Proc Natl Acad Sci U S A* **70**:1677–1681. doi:10.1073/pnas.70.6.1677

Reale E, Luciano L, Spitznas M. 1978. Communicating junctions of the human sensory retina - A freeze-fracture study. *Albr von Graefes Arch für Klin und Exp Ophthalmol* **208**:77–92. doi:10.1007/BF00406984

Ribelayga C, Cao Y, Mangel SC. 2008. The Circadian Clock in the Retina Controls Rod-Cone Coupling. *Neuron* **59**:790–801. doi:10.1016/j.neuron.2008.07.017

Ribelayga C, Mangel SC. 2010. Identification of a circadian clock-controlled neural pathway in the rabbit retina. *PLoS One* **5**. doi:10.1371/journal.pone.0011020

Schneeweis DM, Schnapf JL. 1995. Photovoltage of rods and cones in the macaque retina. *Science (80-)* **268**:1053–1056. doi:10.1126/science.7754386

Sigulinsky CL, Anderson JR, Kerzner E, Rapp CN, Pfeiffer RL, Rodman TM, Emrich DP, Rapp KD, Nelson NT, Scott Lauritzen J, Meyer M, Marc RE, Jones BW. 2020. Network architecture of gap junctional coupling among parallel processing channels in the mammalian retina. *J Neurosci* **40**. doi:10.1523/JNEUROSCI.1810-19.2020

Smith RG, Freed MA, Sterling P. 1986. Microcircuitry of the dark-adapted cat retina: Functional

architecture of the rod-cone network. *J Neurosci* **6**:3505–3517. doi:10.1523/jneurosci.06-12-03505.1986

Söhl G, Odermatt B, Maxeiner S, Degen J, Willecke K. 2004. New insights into the expression and function of neural connexins with transgenic mouse mutants. *Brain Res Brain Res Rev* **47**:245–59. doi:10.1016/j.brainresrev.2004.05.006

Srinivas M, Rozental R, Kojima T, Dermietzel R, Mehler M, Condorelli DF, Kessler JA, Spray DC. 1999. Functional properties of channels formed by the neuronal gap junction protein connexin36. *J Neurosci* **19**:9848–55. doi:10.1523/JNEUROSCI.19-22-09848.1999

Szoboszlay M, Lőrincz A, Lanore F, Vervaeke K, Silver RA, Nusser Z. 2016. Functional Properties of Dendritic Gap Junctions in Cerebellar Golgi Cells. *Neuron* **90**:1043–1056. doi:10.1016/j.neuron.2016.03.029

Teubner B, Degen J, Söhl G, Güldenagel M, Bukauskas FF, Trexler EB, Verselis VK, De Zeeuw CI, Lee CG, Kozak CA, Petrasch-Parwez E, Dermietzel R, Willecke K. 2000. Functional Expression of the Murine Connexin 36 Gene Coding for a Neuron-Specific Gap Junctional Protein. *J Membr Biol* **176**:249–262. doi:10.1007/s00232001094

Tsukamoto Y, Morigiwa K, Ueda M, Sterling P. 2001. Microcircuits for night vision in mouse retina. *J Neurosci* **21**:8616–8623. doi:10.1523/jneurosci.21-21-08616.2001

Whitaker CM, Nobles G, Ishibashi M, Massey SC. 2021. Rod and Cone Connections With Bipolar Cells in the Rabbit Retina. *Front Cell Neurosci* **15**. doi:10.3389/FNCEL.2021.662329

Xu CS, Hayworth KJ, Lu Z, Grob P, Hassan AM, García-Cerdán JG, Niyogi KK, Nogales E, Weinberg RJ, Hess HF. 2017. Enhanced FIB-SEM systems for large-volume 3D imaging. *Elife* **6**:1–36. doi:10.7554/eLife.25916

1708 Zhang J, Wu SM. 2004. Connexin35/36 Gap Junction Proteins Are Expressed in Photoreceptors
1709 of the Tiger Salamander Retina. *J Comp Neurol* **470**:1–12. doi:10.1002/cne.10967
1710

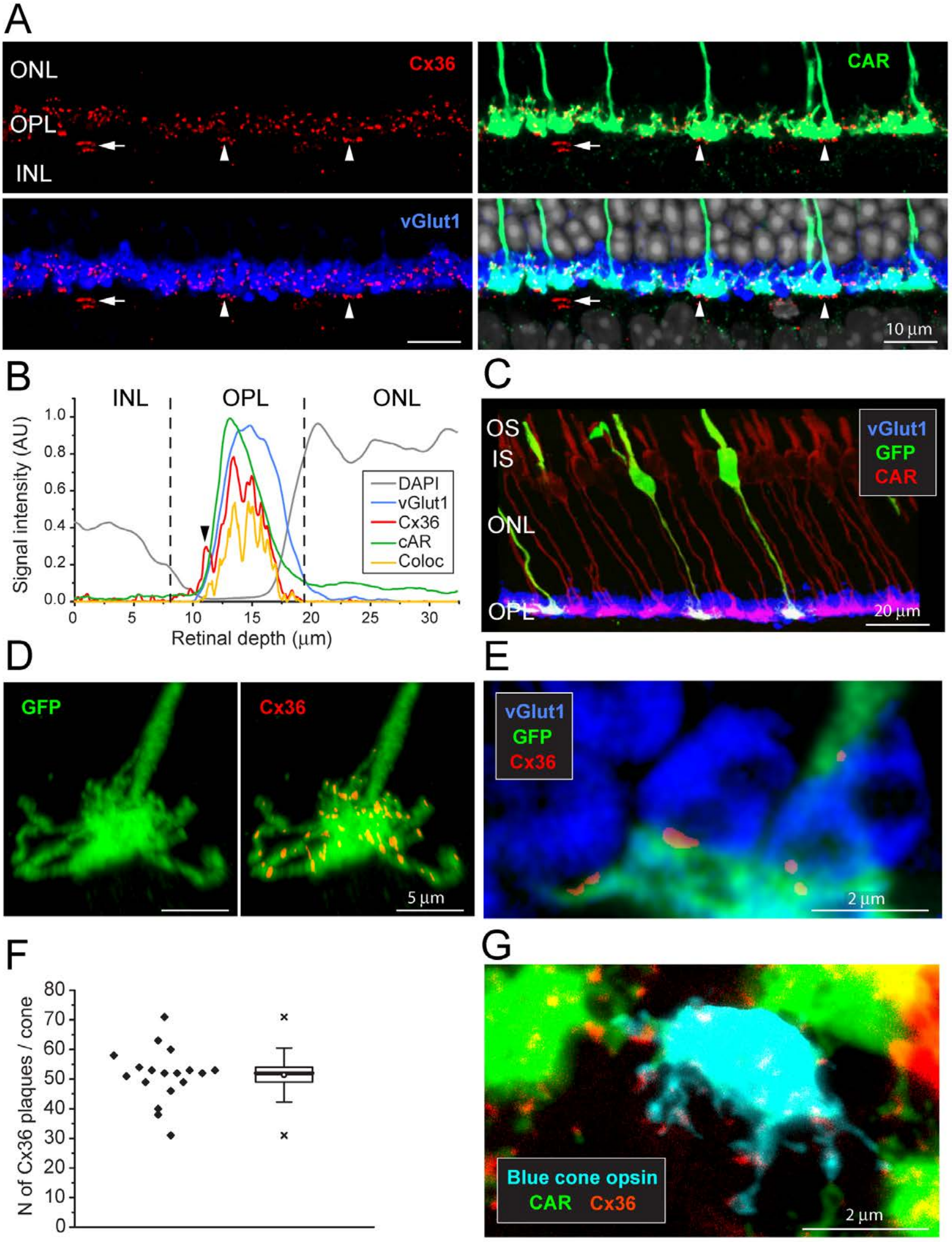
A
ONL
OPL
INL
Cx36
CAR
vGlut1
10 µm
B
INL
OPL
ONL
Signal intensity (AU)
Retinal depth (µm)
DAPI
vGlut1
Cx36
cAR
Coloc
C
OS
IS
ONL
OPL
vGlut1
GFP
CAR
20 µm
D
GFP
Cx36
5 µm
E
vGlut1
GFP
Cx36
2 µm
F
N of Cx36 plaques / cone
G
Blue cone opsin
CAR Cx36
2 µm

A

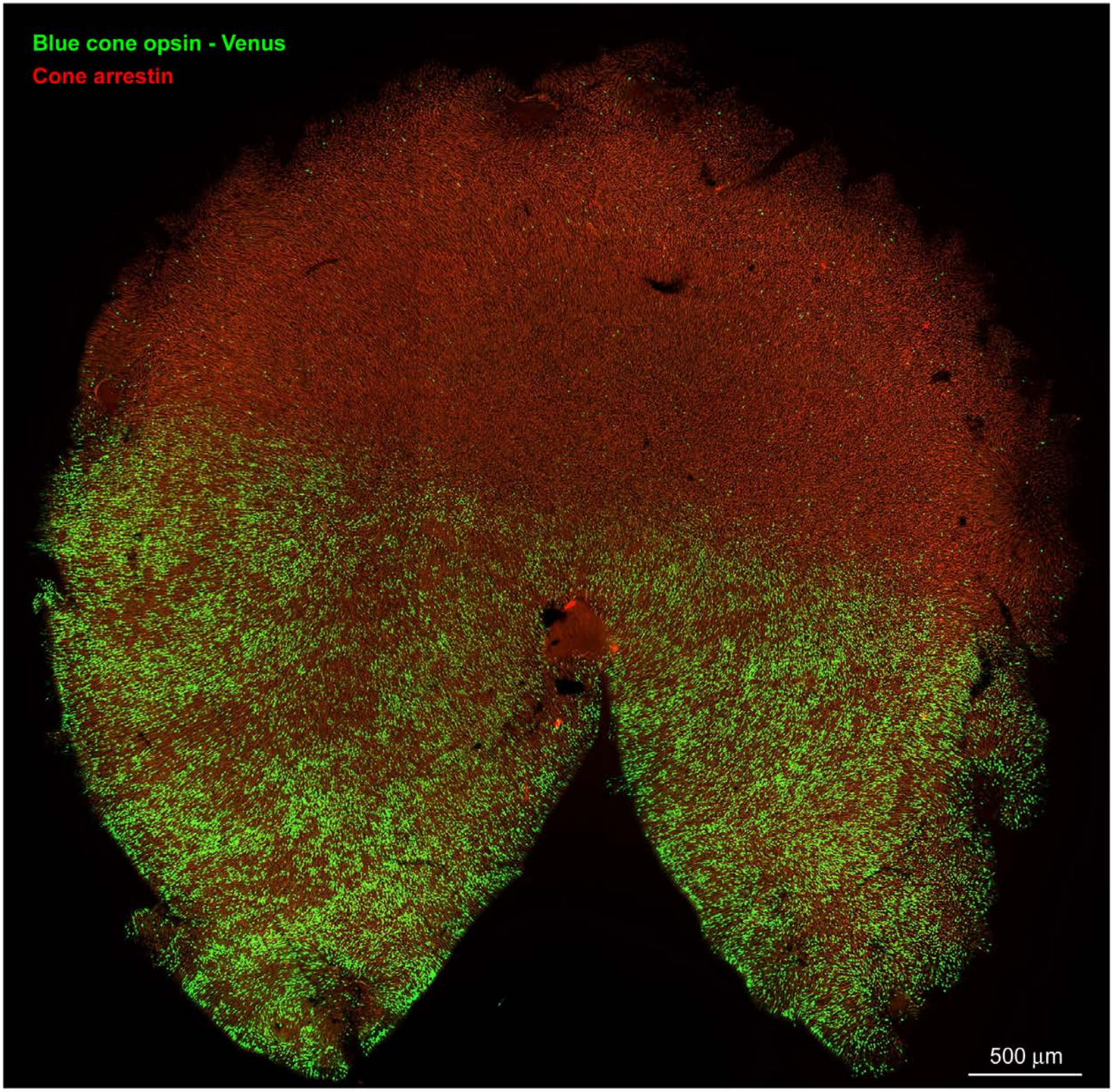
Blue cone opsin - Venus
Cone arrestin
500 µm

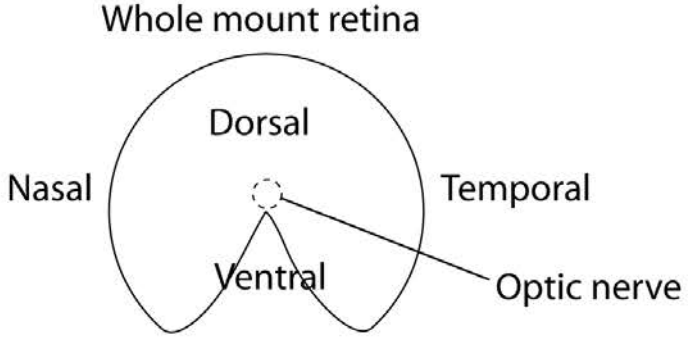
Whole mount retina
Dorsal
Nasal
Temporal
Ventral
Optic nerve

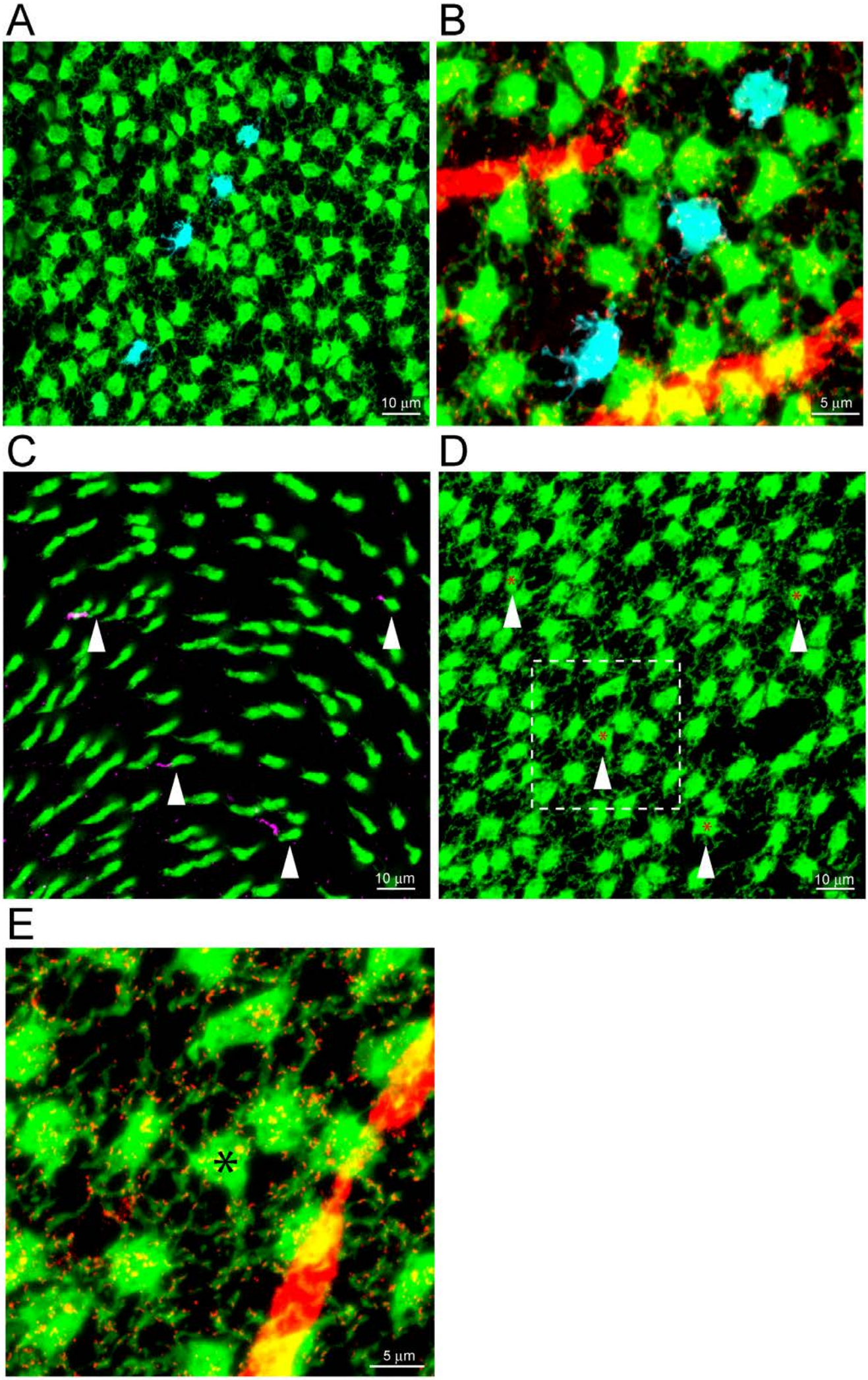
A
10 µm
B
5 µm
C
10 µm
D
10 µm
E
5 µm

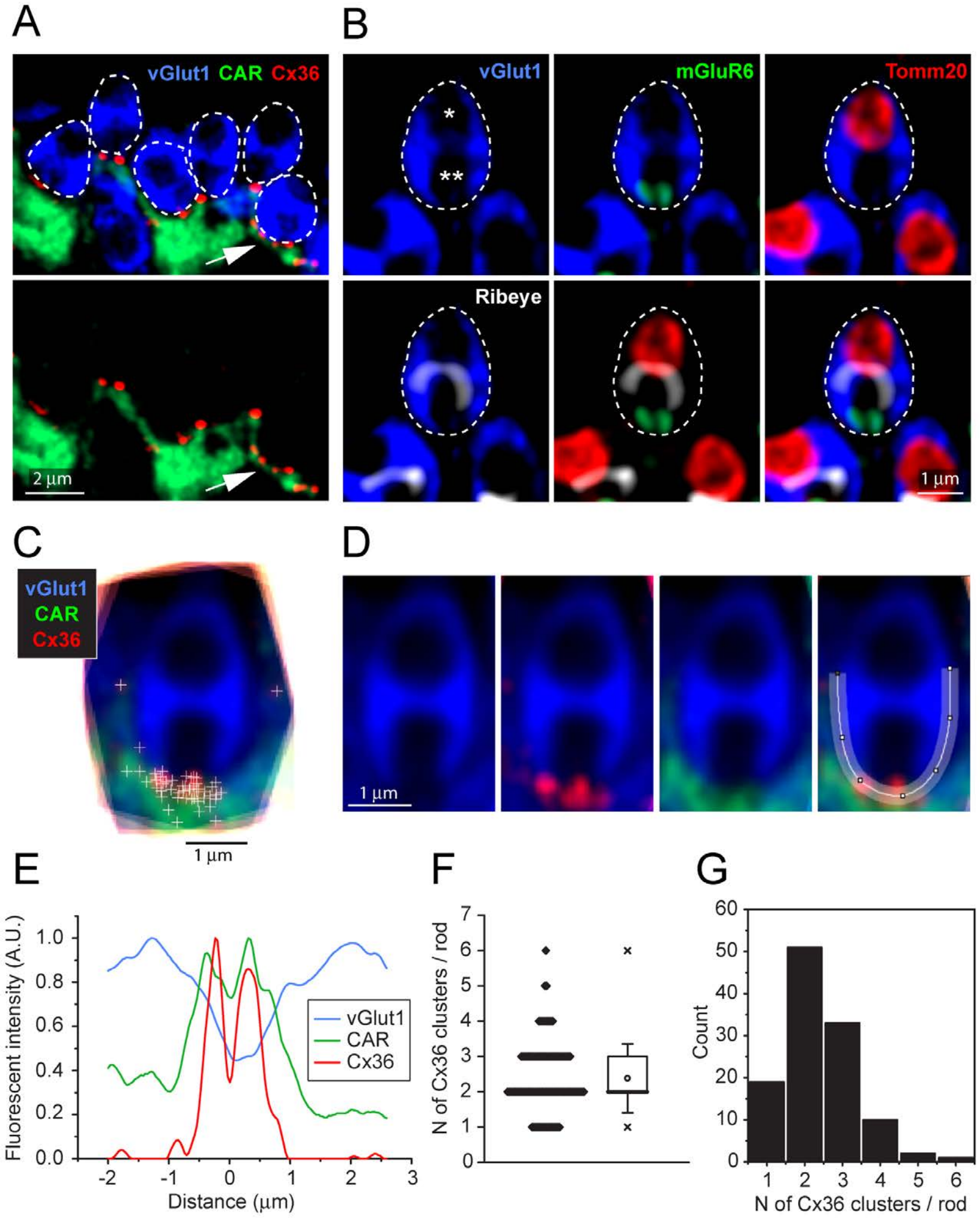
A
vGlut1 CAR Cx36
2 µm
B
vGlut1
mGluR6
Tomm20
*
**
Ribeye
1 µm
C
vGlut1
CAR
Cx36
1 µm
D
1 µm
E
Fluorescent intensity (A.U.)
Distance (µm)
vGlut1
CAR
Cx36
F
N of Cx36 clusters / rod
G
Count
N of Cx36 clusters / rod

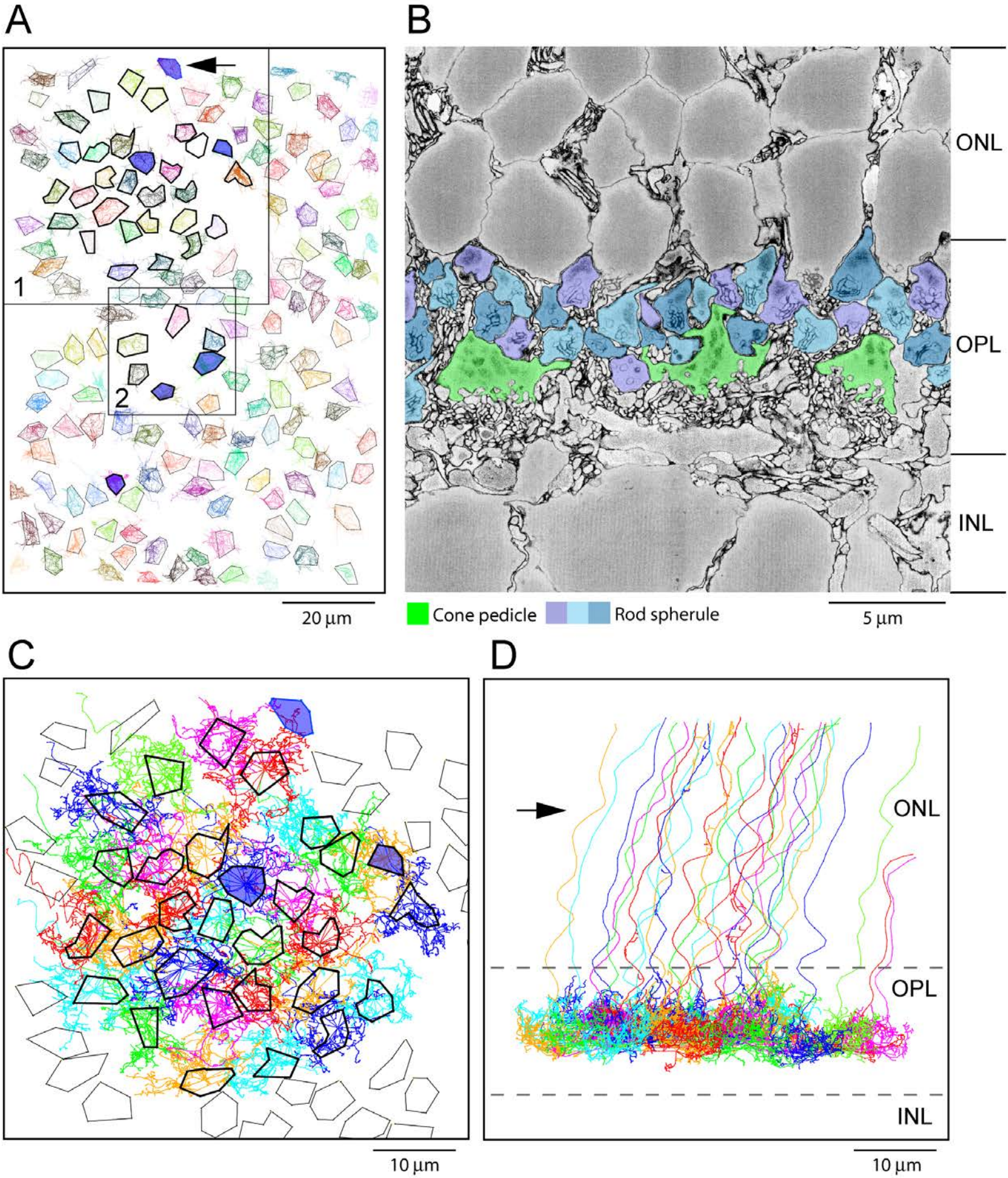
A
1
2
20 µm
B
ONL
OPL
INL
Cone pedicle
Rod spherule
5 µm
C
10 µm
D
ONL
OPL
INL
10 µm

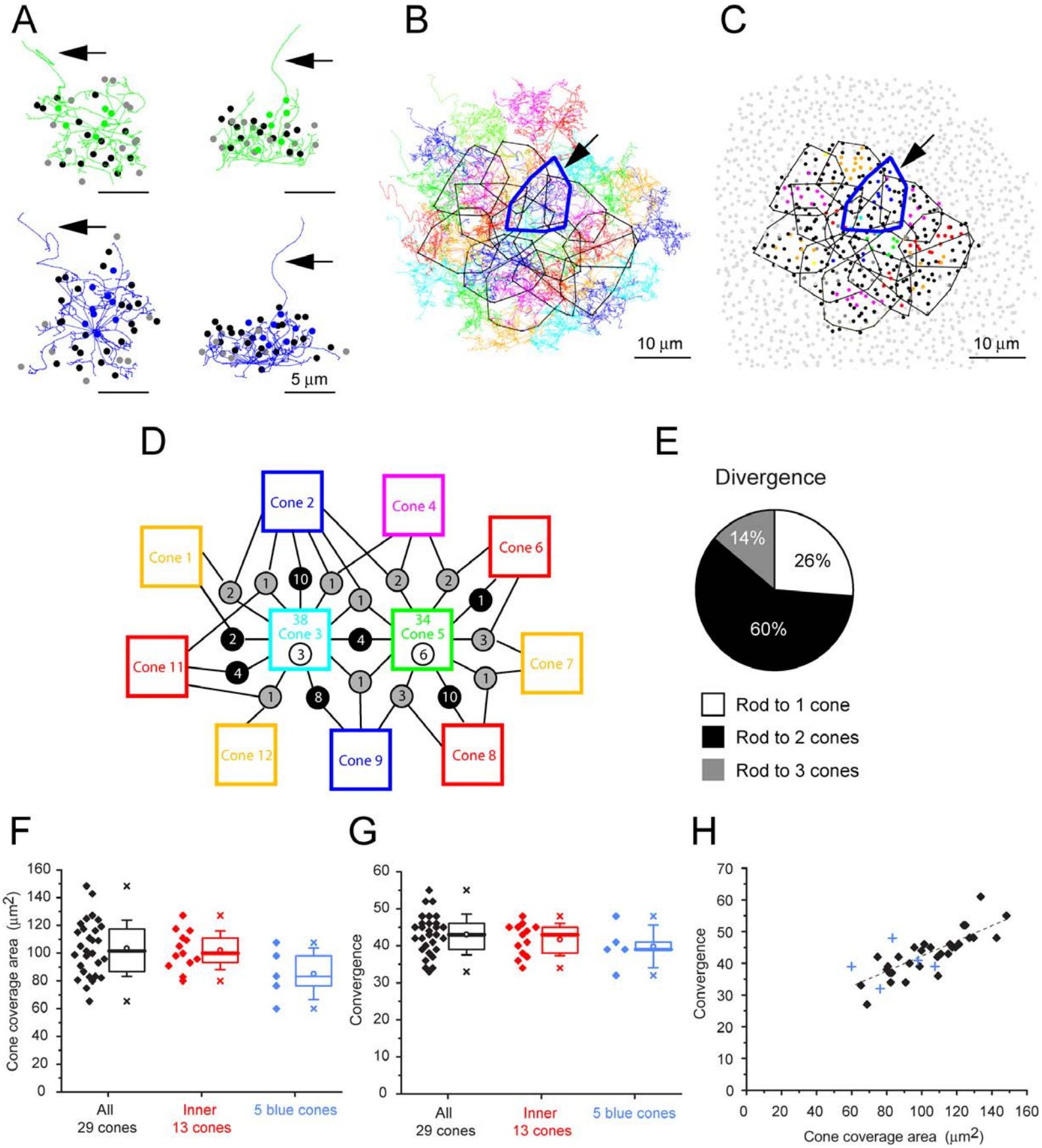
A
5 µm
B
10 µm
C
10 µm
D
Cone 1
Cone 2
Cone 4
Cone 6
Cone 7
Cone 8
Cone 9
Cone 11
Cone 12
38
Cone 3
34
Cone 5
E
Divergence
14%
26%
60%
Rod to 1 cone
Rod to 2 cones
Rod to 3 cones
F
Cone coverage area (µm2)
All
29 cones
Inner
13 cones
5 blue cones
G
Convergence
All
29 cones
Inner
13 cones
5 blue cones
H
Convergence
Cone coverage area (µm2)

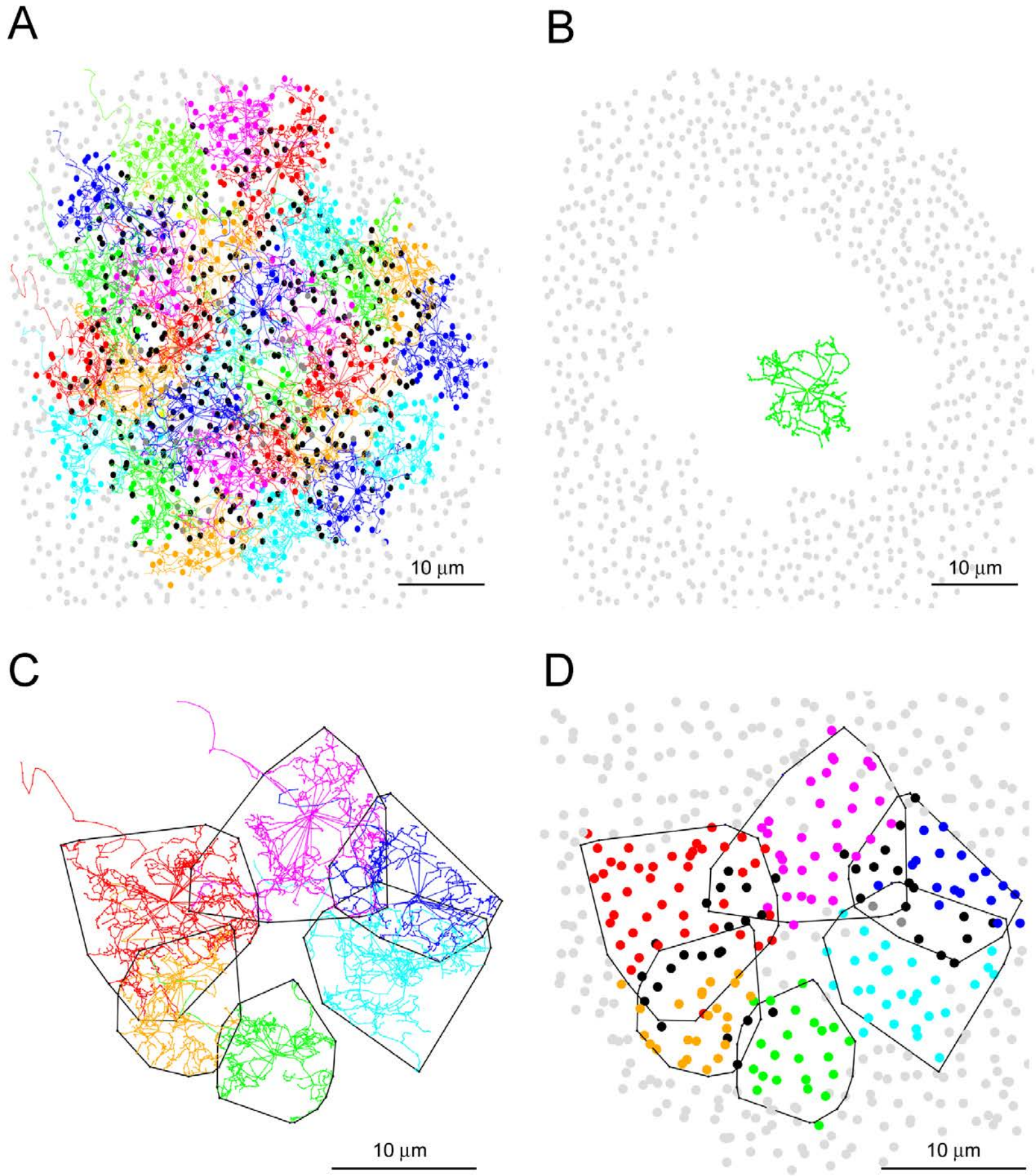
A
10 µm
B
10 µm
C
10 µm
D
10 µm

A

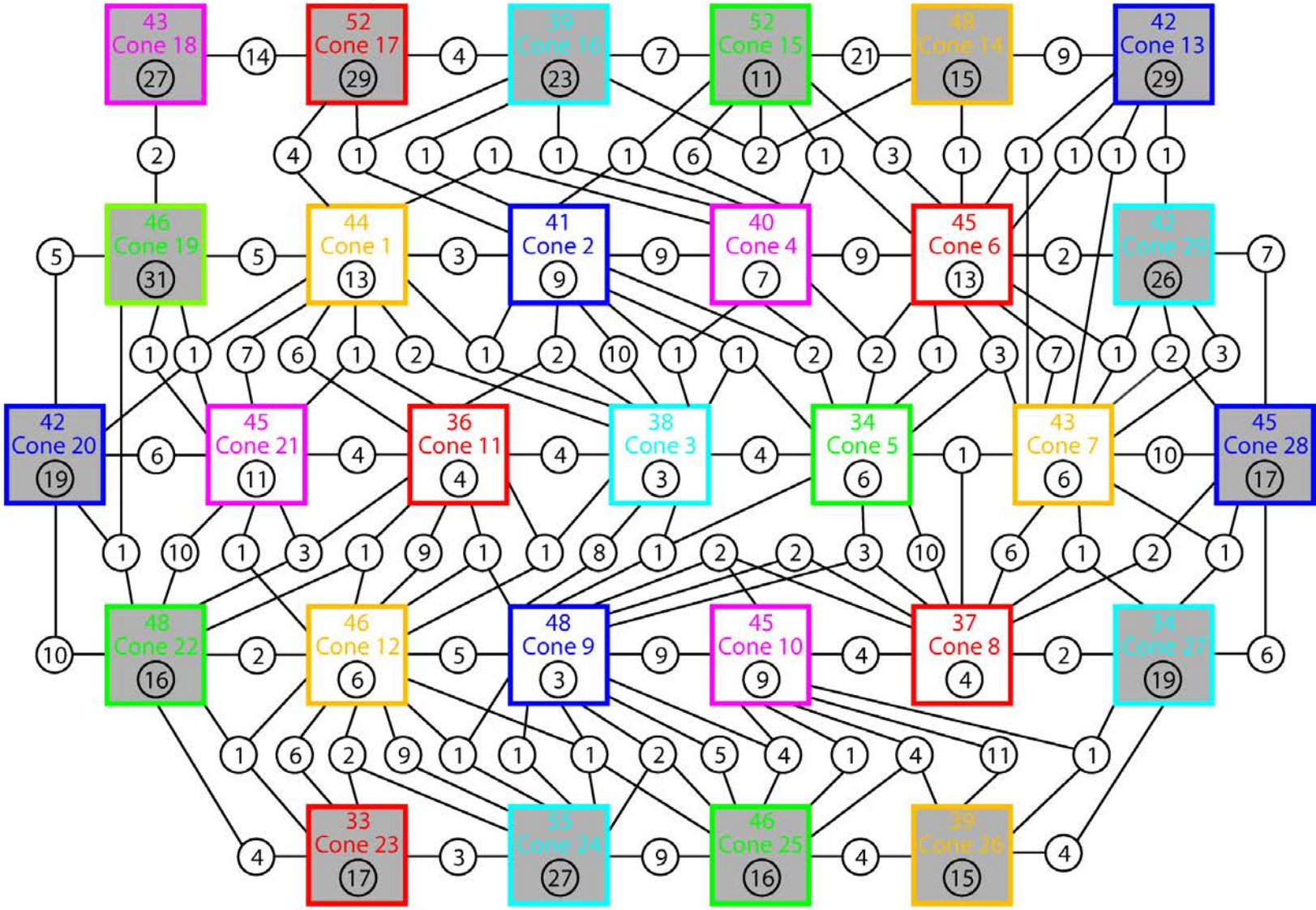
43 Cone 18 27
52 Cone 17 29
39 Cone 16 23
52 Cone 15 11
48 Cone 14 15
42 Cone 13 29
46 Cone 19 31
44 Cone 1 13
41 Cone 2 9
40 Cone 4 7
45 Cone 6 13
42 Cone 29 26
42 Cone 20 19
45 Cone 21 11
36 Cone 11 4
38 Cone 3 3
34 Cone 5 6
43 Cone 7 6
45 Cone 28 17
48 Cone 22 16
46 Cone 12 6
48 Cone 9 3
45 Cone 10 9
37 Cone 8 4
34 Cone 27 19
33 Cone 23 17
55 Cone 24 27
46 Cone 25 16
39 Cone 26 15

B

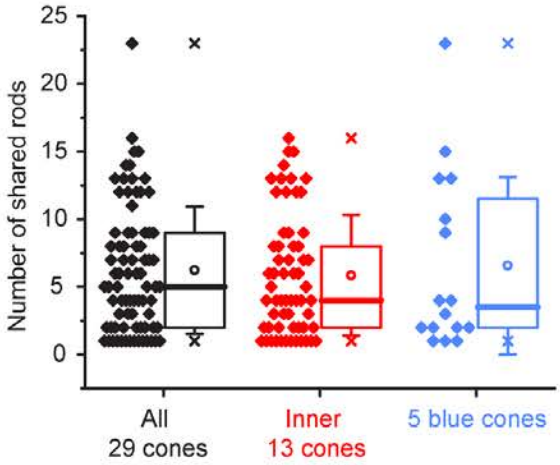
Number of shared rods
25
20
15
10
5
0
All
29 cones
Inner
13 cones
5 blue cones

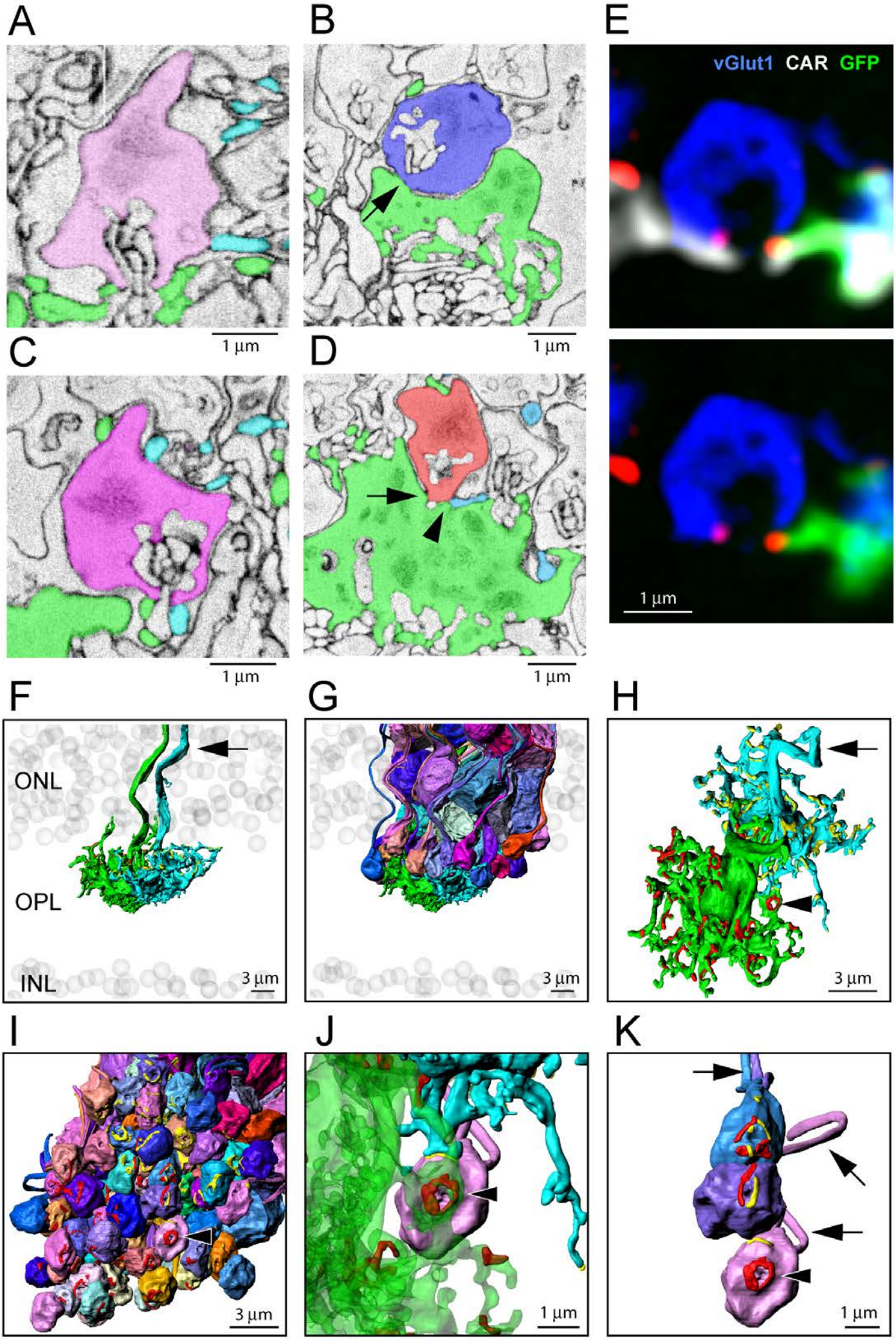
A
B
E
vGlut1
CAR
GFP
1 µm
1 µm
C
D
1 µm
1 µm
1 µm
F
G
H
ONL
OPL
INL
3 µm
3 µm
3 µm
I
J
K
3 µm
1 µm
1 µm

A

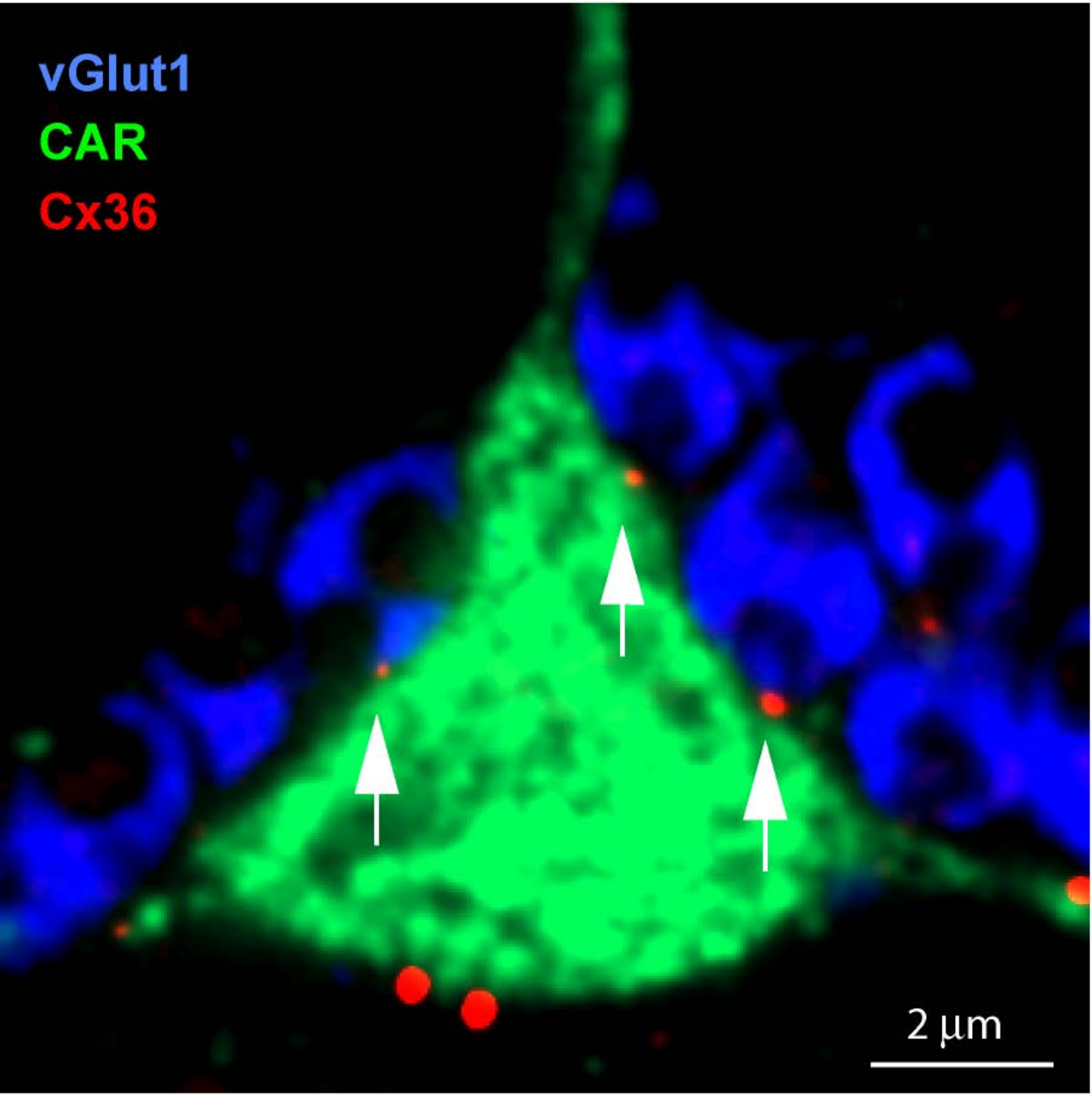

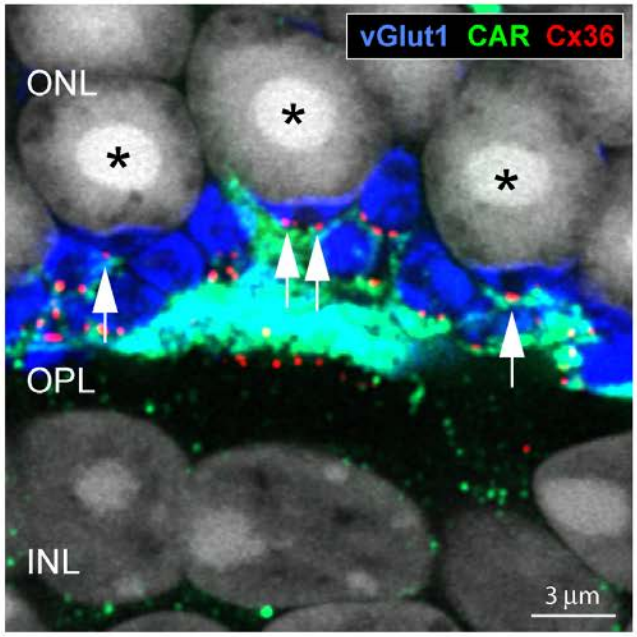
A
vGlut1 CAR Cx36
ONL
OPL
INL
3 µm

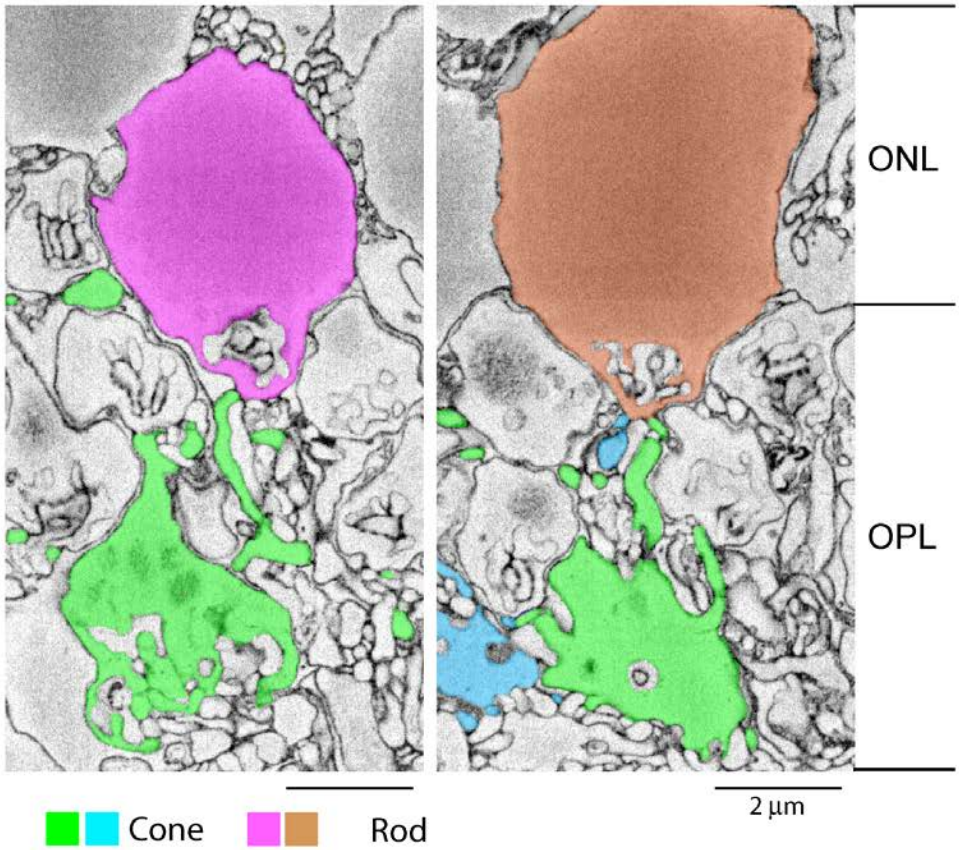
B
ONL
OPL
2 µm
Cone
Rod

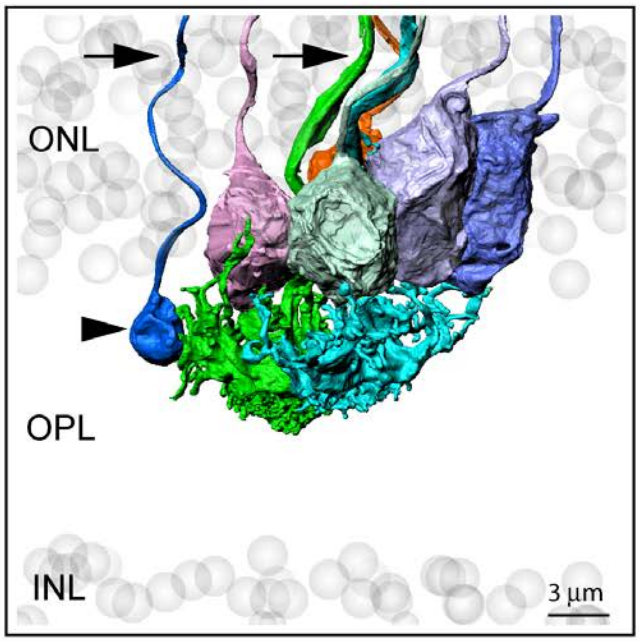
C
ONL
OPL
INL
3 µm

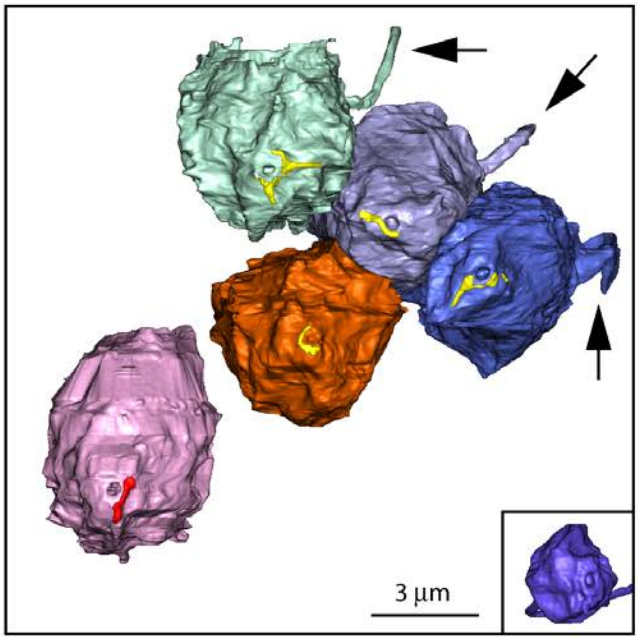
D
3 µm

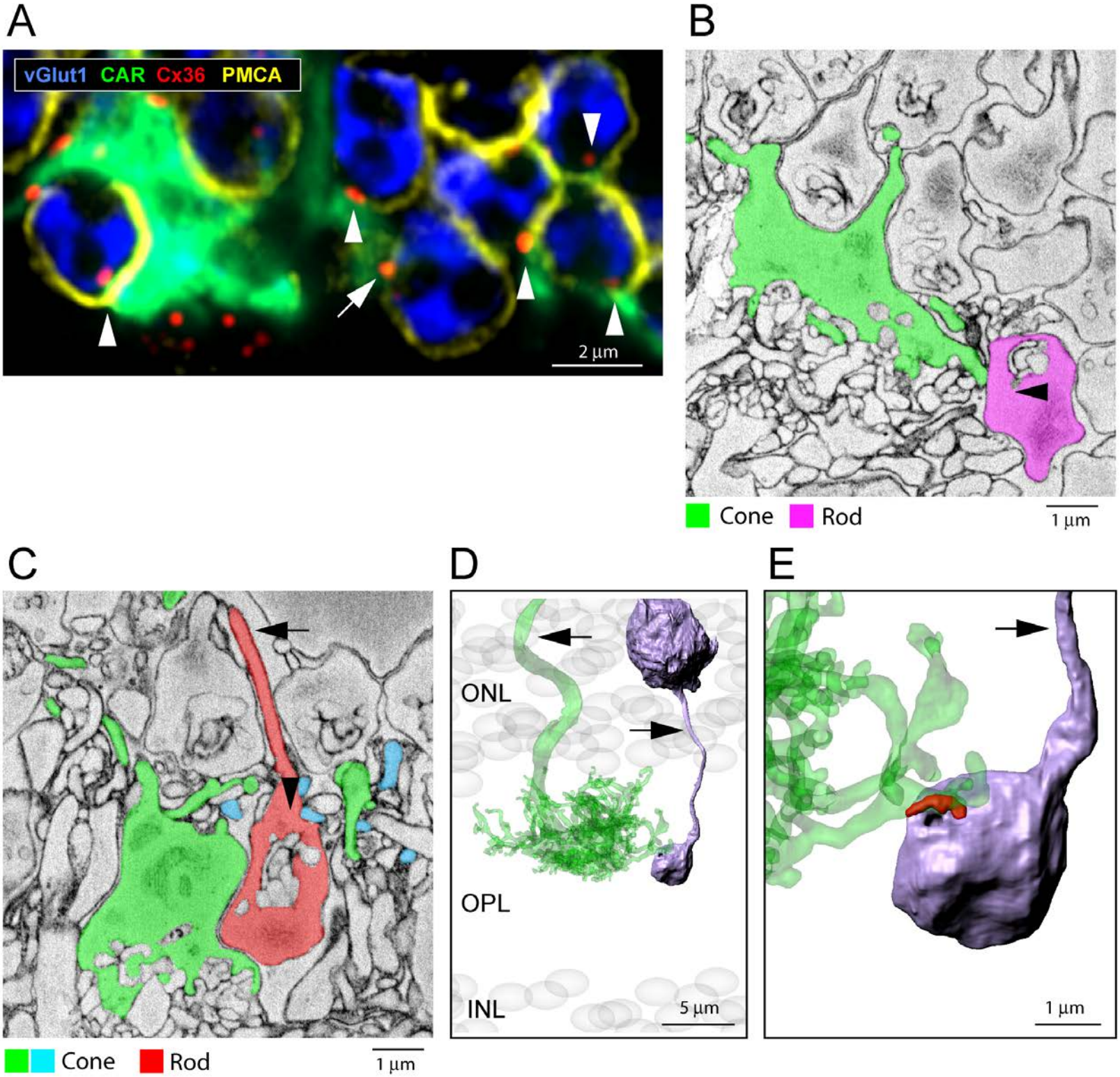
A
vGlut1 CAR Cx36 PMCA
2 µm
B
Cone
Rod
1 µm
C
Cone
Rod
1 µm
D
ONL
OPL
INL
5 µm
E
1 µm

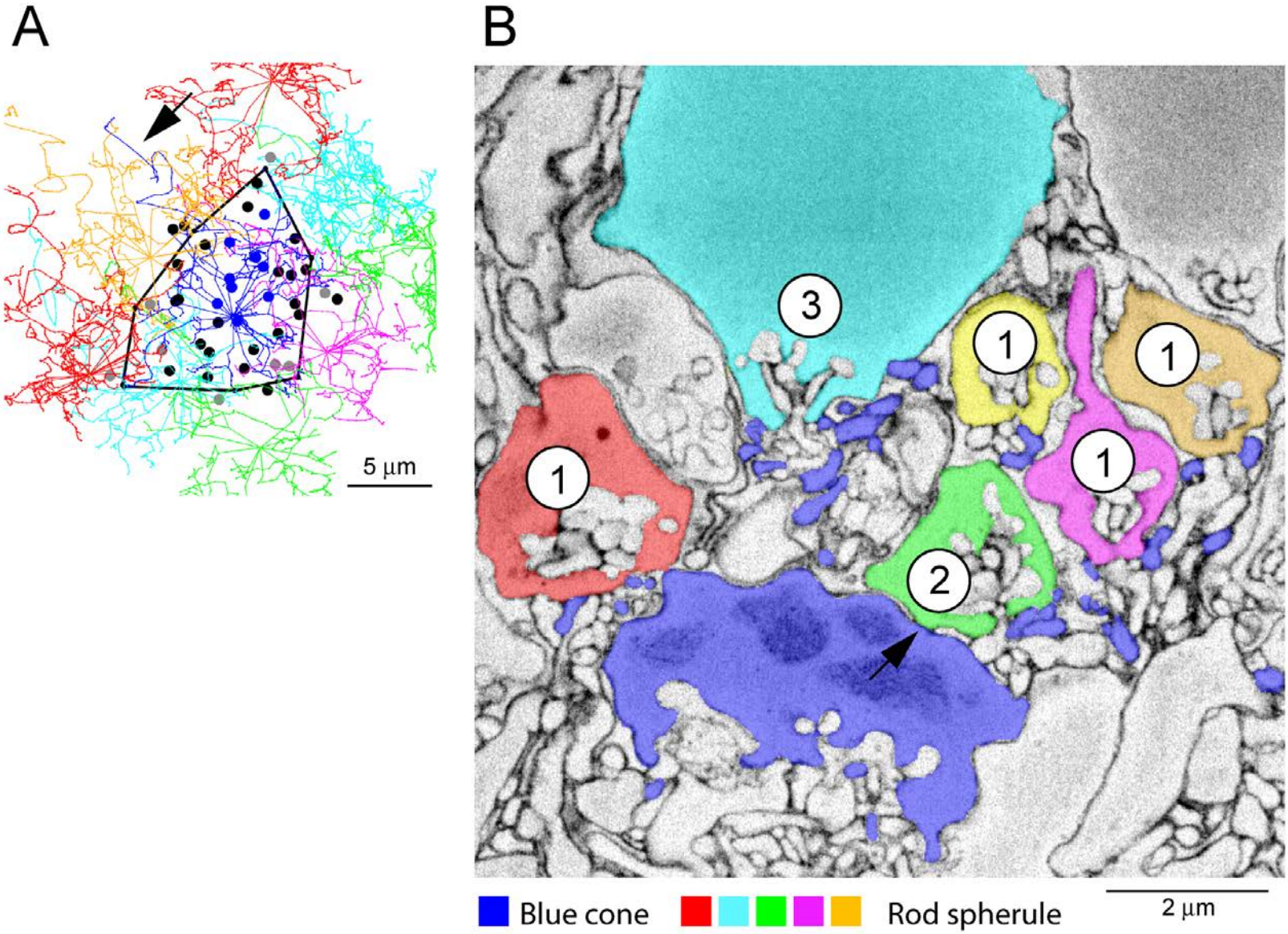
A
5 µm
B
3
1
1
1
1
2
Blue cone
Rod spherule
2 µm

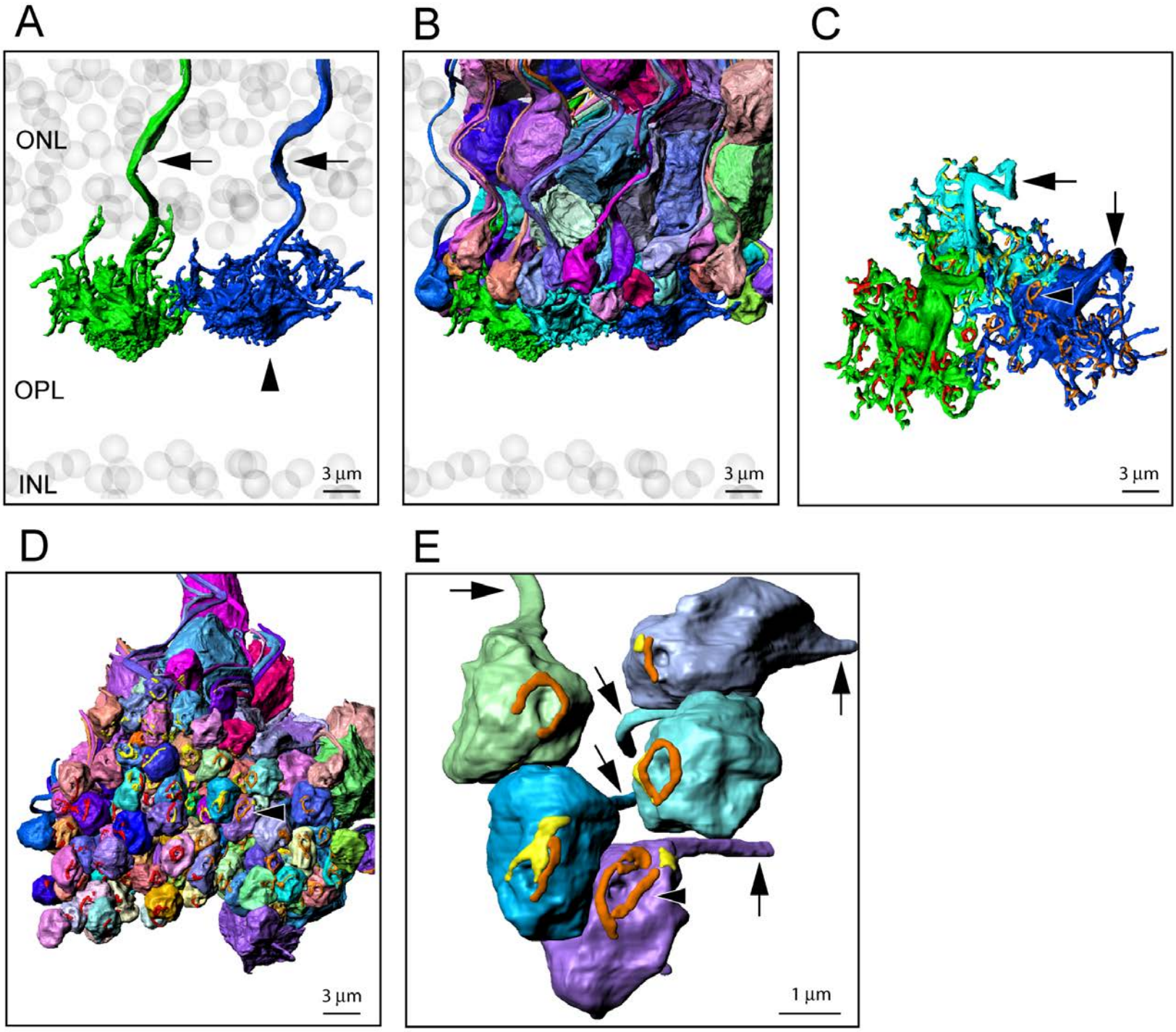
A
ONL
OPL
INL
3 µm
B
3 µm
C
3 µm
D
3 µm
E
1 µm

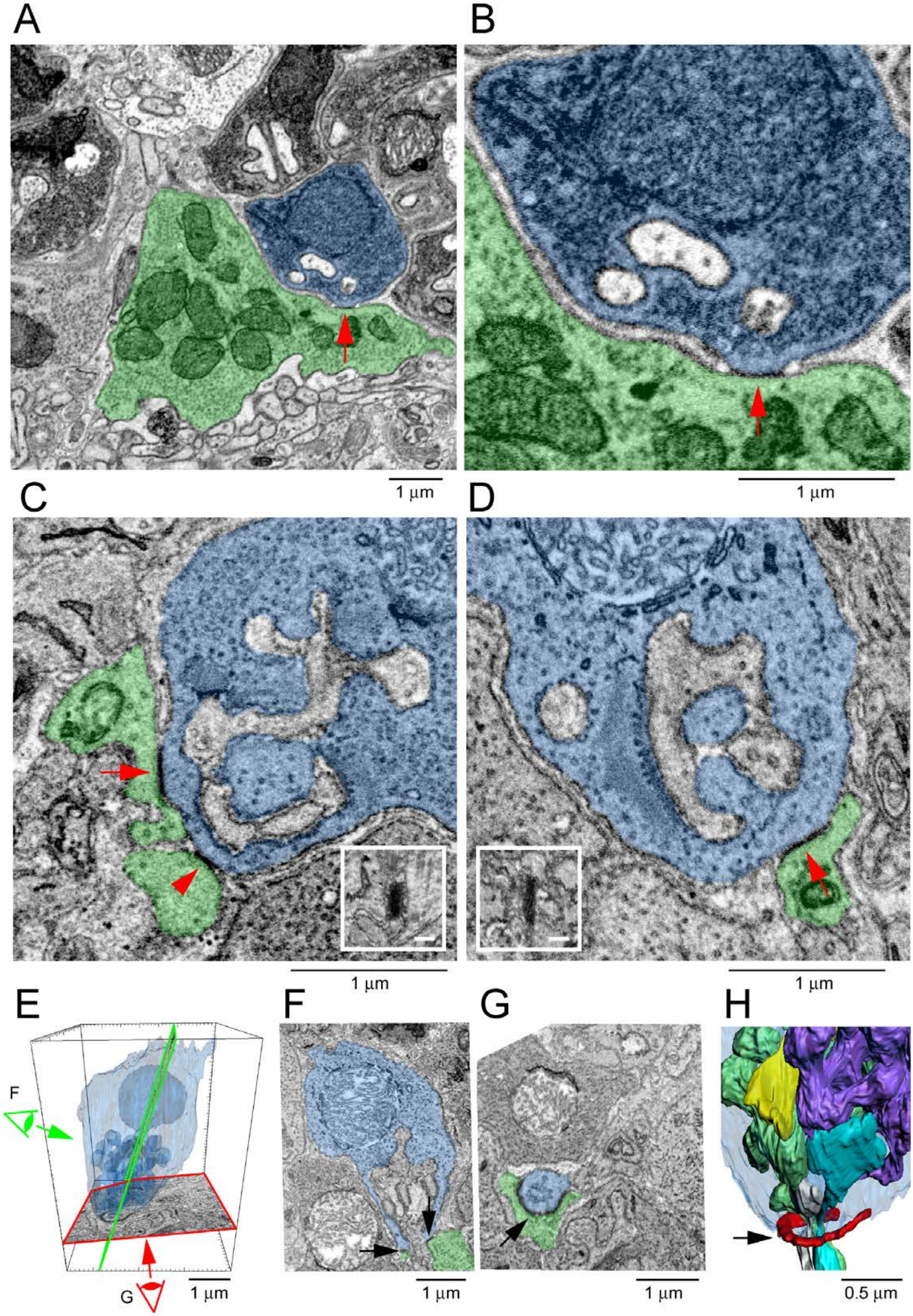
A
B
1 µm
1 µm
C
D
1 µm
1 µm
E
F
G
1 µm
F
1 µm
G
1 µm
H
0.5 µm

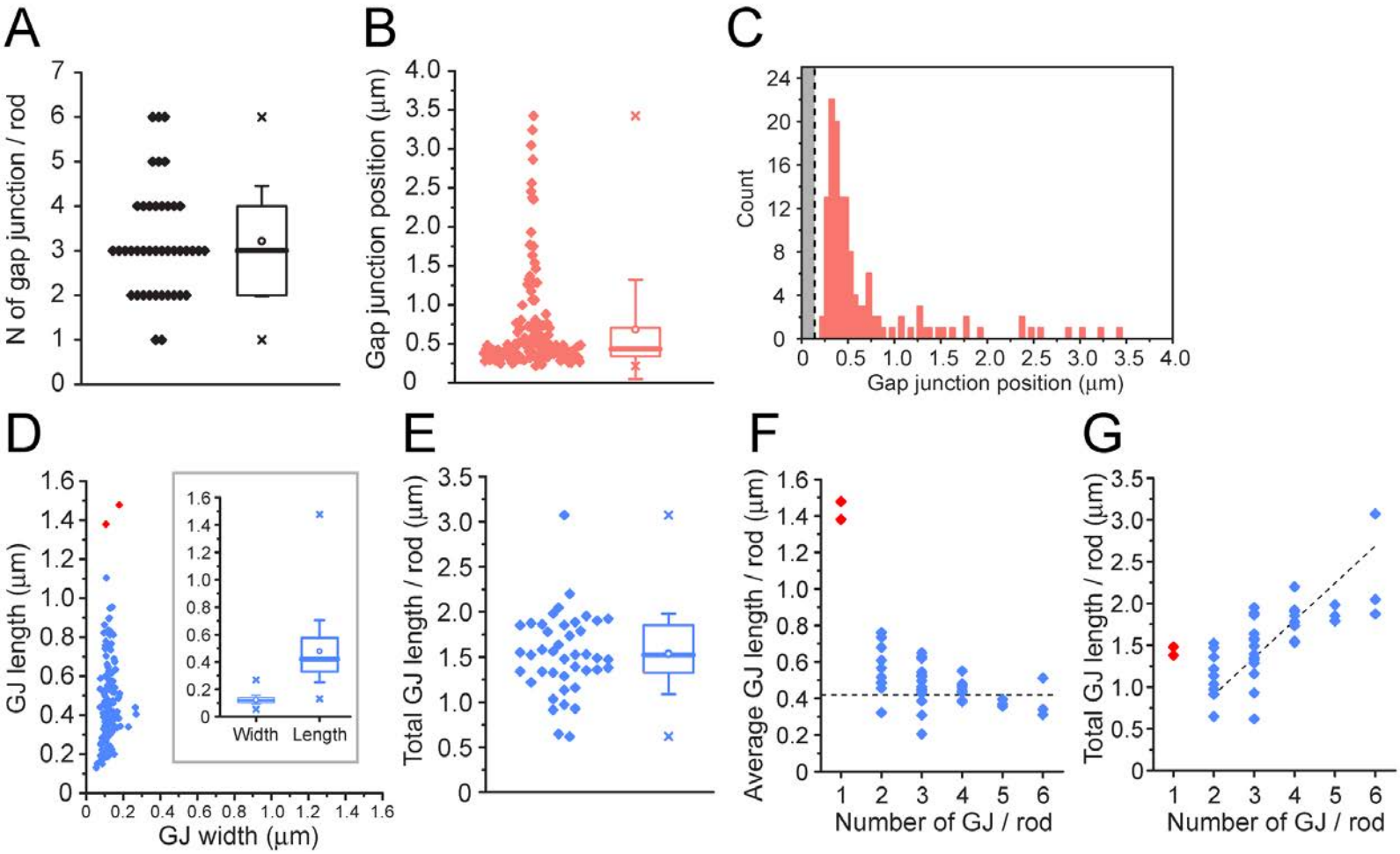
A
N of gap junction / rod
B
Gap junction position (µm)
C
Count
Gap junction position (µm)
D
GJ length (µm)
GJ width (µm)
Width
Length
E
Total GJ length / rod (µm)
F
Average GJ length / rod (µm)
Number of GJ / rod
G
Total GJ length / rod (µm)
Number of GJ / rod

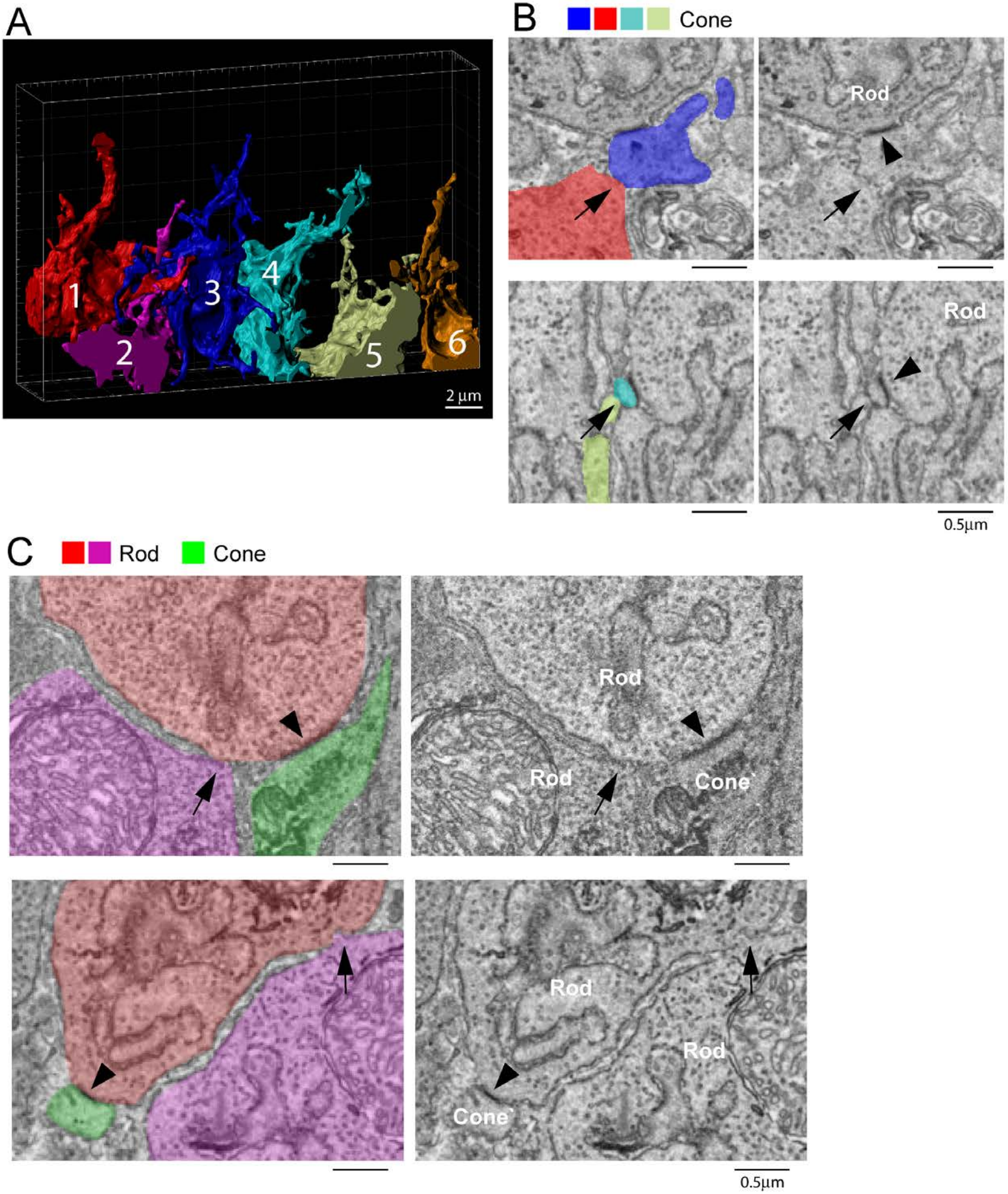
A
1
2
3
4
5
6
2 µm
B
Cone
Rod
Rod
0.5µm
C
Rod
Cone
Rod
Rod
Cone
Rod
Rod
Cone
0.5µm

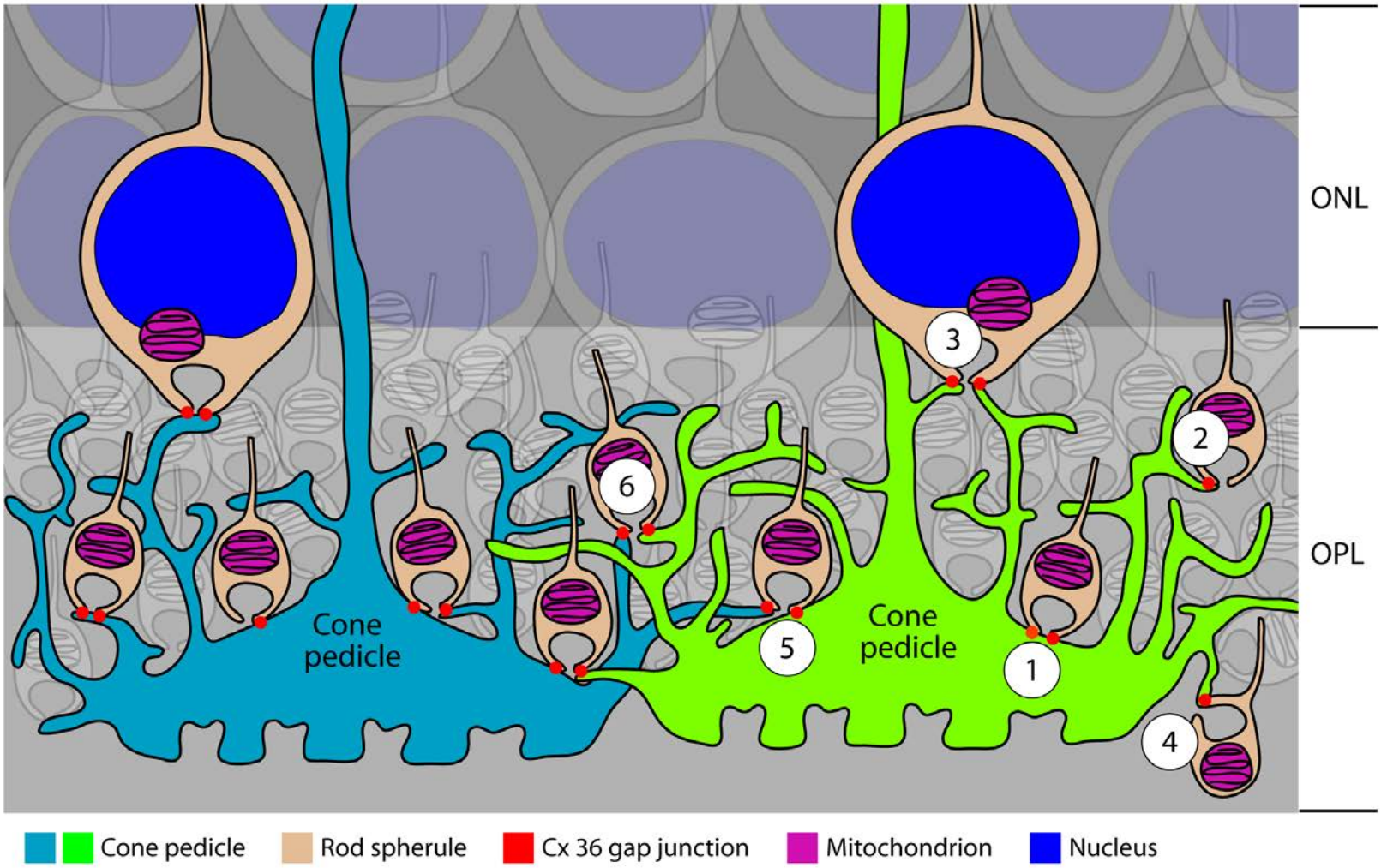

Rod - Cone Coupling

1. Roof contact
2. Telodendron contact
3. Telodendria contact to low rod soma
4. Telodendron contact to low rod spherule

Rod - Multiple Cones Coupling

5. Roof & telodendron contact
6. Telodendria contact